



## The Impact of SST Biases in the Tropical East Pacific and Agulhas Current Region on Atmospheric Stationary Waves in the Southern Hemisphere

CHAIM I. GARFINKEL AND IAN WHITE

*Fredy and Nadine Herrmann Institute of Earth Sciences, Hebrew University of Jerusalem, Jerusalem, Israel*

EDWIN P. GERBER

*Courant Institute of Mathematical Sciences, New York University, New York, New York*

MARTIN JUCKER

*Climate Change Research Centre and ARC Centre of Excellence for Climate Extremes, University of New South Wales, Sydney, Australia*

(Manuscript received 22 March 2020, in final form 21 July 2020)

**ABSTRACT:** Climate models in phase 5 of the Coupled Model Intercomparison Project (CMIP5) vary significantly in their ability to simulate the phase and amplitude of atmospheric stationary waves in the midlatitude Southern Hemisphere. These models also suffer from a double intertropical convergence zone (ITCZ), with excessive precipitation in the tropical eastern South Pacific, and many also suffer from a biased simulation of the dynamics of the Agulhas Current around the tip of South Africa. The intermodel spread in the strength and phasing of SH midlatitude stationary waves in the CMIP archive is shown to be significantly correlated with the double-ITCZ bias and biases in the Agulhas Return Current. An idealized general circulation model (GCM) is used to demonstrate the causality of these links by prescribing an oceanic heat flux out of the tropical east Pacific and near the Agulhas Current. A warm bias in tropical east Pacific SSTs associated with an erroneous double ITCZ leads to a biased representation of midlatitude stationary waves in the austral hemisphere, capturing the response evident in CMIP models. Similarly, an overly diffuse sea surface temperature gradient associated with a weak Agulhas Return Current leads to an equatorward shift of the Southern Hemisphere jet by more than 3° and weak stationary wave activity in the austral hemisphere. Hence, rectification of the double-ITCZ bias and a better representation of the Agulhas Current should be expected to lead to an improved model representation of the austral hemisphere.

**KEYWORDS:** Intertropical convergence zone; Stationary waves; Boundary currents

### 1. Introduction

Policy makers and stakeholders rely on projections of anthropogenic climate change in order to justify mitigation efforts and plan adaptation measures. The main tool for producing such projections are coupled ocean–atmosphere models used in climate assessments, such as the Coupled Model Intercomparison Project (CMIP). However, these projections differ among models even when identical forcings

are applied, with across-model differences particularly pronounced on regional scales (Knutti and Sedláček 2013; He and Soden 2016; Garfinkel et al. 2020a), despite substantial model development (e.g., better model physics) and ever-increasing computational capacity (finer resolution).

The past few generations of CMIP models suffer from large biases in their climatology of precipitation in the tropical South Pacific and in the Southern Hemisphere storm tracks and stationary waves. There is evidence that these biases lead to spread and uncertainty in future projections. Specifically, many aspects of the changes in regional climate depend upon the unperturbed climatology (e.g., Held and Soden 2006; Matsueda and Palmer 2011; Scheff and Frierson 2012), and hence climatological biases could lead to unrealistic projections of anthropogenic climate change (Matsueda and Palmer 2011; He and Soden 2016). This limits the utility of projections of regional climate change from CMIP models.

The climate of Earth is decidedly not zonally symmetric, even in the Southern Hemisphere. These zonal asymmetries, or stationary waves, are forced by asymmetries in the lower boundary, such as orography and the land–ocean distribution.

 Denotes content that is immediately available upon publication as open access.

 Supplemental information related to this paper is available at the Journals Online website: <https://doi.org/10.1175/JCLI-D-20-0195.s1>.

*Corresponding author:* Chaim I. Garfinkel, [chaim.garfinkel@mail.huji.ac.il](mailto:chaim.garfinkel@mail.huji.ac.il)

DOI: 10.1175/JCLI-D-20-0195.1

© 2020 American Meteorological Society. For information regarding reuse of this content and general copyright information, consult the [AMS Copyright Policy \(www.ametsoc.org/PUBSReuseLicenses\)](#).

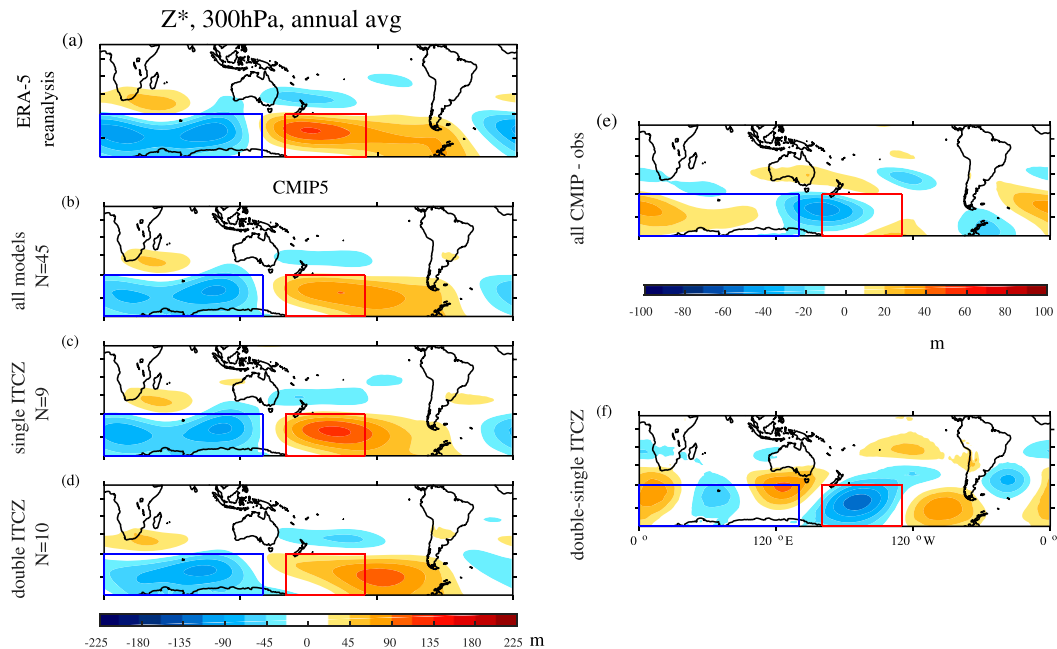


FIG. 1. Climatology of deviations of geopotential height at 300 hPa from the zonal mean in the annual average in (a) ERA5 reanalysis. (b) As in (a), but in the 45 CMIP5 listed in Table 1; (c) as in (b), but in models with a relatively small double-ITCZ bias, defined here as simulating precipitation in the region 17°–2°S, 190°–250°E less than 175% of the observed value (excluding MIROC models); (d) as in (b), but in models with a relatively large double-ITCZ bias, defined here as simulating more than 250% of the observed value of precipitation in the region 17°–2°S, 190°–250°E; (e) difference between (b) and (a) [i.e., (b) – (a)]; and (f) difference between (d) and (c) [i.e., (d) – (c)]. The contour interval is 22.5 m for (a)–(d) and 10 m for (e) and (f).

Stationary waves control, in large part, the zonal structure of storm tracks (e.g., Inatsu and Hoskins 2004), which are closely linked to extreme wind and precipitation events (Shaw et al. 2016). Subtle shifts in stationary waves, such as those projected to occur under climate change (Wang et al. 2013; Simpson et al. 2014), can lead to profound impacts on regional climate.

The Southern Hemisphere stationary wave pattern is dominated by zonal wavenumber 1 at both tropospheric and stratospheric levels (James 1988; Quintanar and Mechoso 1995a) with a ridge in the Pacific Ocean sector and a trough south of Africa and in the Indian Ocean sector (Fig. 1a). The amplitude of this wave is largest at about 60°S and is most pronounced during September and October in the upper troposphere and stratosphere (Quintanar and Mechoso 1995a). This stationary wave pattern is driven in part by Antarctic orography (James 1988), but with a more important contribution from a wave train propagating out of the tropical Indian Ocean with a ridge in the subtropical south Indian Ocean, a trough in the Indian sector of the Southern Ocean, and a ridge south of New Zealand (Quintanar and Mechoso 1995a,b; Fig. 1a). This wave train is associated with the large-scale convective maxima that extends from the tropical northwestern Pacific to India (Inatsu and Hoskins 2004). Stronger convection in this region on interannual time scales is associated with a stronger stationary wave pattern (Peña-Ortiz et al. 2019). Southern Hemisphere stationary waves are also sensitive to frictional drag, with stronger drag leading to a stronger wave-1 pattern via transient eddies (Garfinkel et al. 2013a).

Comprehensive climate models simulate a wide range of amplitudes and phases of this stationary wave pattern (Figs. 4.5–4.7 of Eyring et al. 2010), with some models simulating stationary waves twice as strong as observed and others with a phase difference of nearly 180° relative to those observed. The multimodel mean of stationary waves in 45 phase 5 of CMIP (CMIP5) models is shown in Fig. 1b, and it is clear that stationary waves are too weak, with biases largest south of Australia and in the Atlantic Ocean sector (Fig. 1e). Biased stationary waves affect not only near-surface winds and temperature advection (among other impacts) but also long-term climate prediction. Many models suffer from a too-strong stratospheric springtime polar vortex (e.g., Eyring et al. 2010), with subsequent biases in the representation of the ozone and its downward impact (Lin et al. 2017). While some of this bias may be mitigated by improving the representation of gravity waves (McLandress et al. 2012; Alexander and Grimsdell 2013; Garfinkel and Oman 2018), a poor representation of large-scale Rossby waves, which are nominally resolved by the model, also contributes to this bias (Hurwitz et al. 2010; Garfinkel et al. 2013a).

In this study, we employ an idealized atmospheric general circulation model to explore the factors leading to biases in the midlatitude Southern Hemisphere stationary wave pattern. We focus on three systematic biases evident in many CMIP models.

TABLE 1. List of models used.

|    |                 |    |               |    |                |
|----|-----------------|----|---------------|----|----------------|
| 1  | ACCESS1.0       | 2  | ACCESS1.3     | 3  | BNU-ESM        |
| 4  | CCSM4           | 5  | CESM1-BGC     | 6  | CESM1-CAM5     |
| 7  | CESM1(FASTCHEM) | 8  | CESM1-WACCM   | 9  | CMCC-CESM      |
| 10 | CMCC-CM         | 11 | CMCC-CMS      | 12 | CNRM-CM5       |
| 13 | CNRM-CM5.2      | 14 | CSIRO Mk3.6-0 | 15 | CanCM4         |
| 16 | CanESM2         | 17 | FGOALS-g2     | 18 | FIO-ESM        |
| 19 | GFDL CM2p1      | 20 | GFDL CM3      | 21 | GFDL-ESM2G     |
| 22 | GFDL-ESM2M      | 23 | GISS-E2-H     | 24 | GISS-E2-H-CO   |
| 25 | GISS-E2-R       | 26 | GISS-E2-R-CC  | 27 | HadCM3         |
| 28 | HadGEM2-AO      | 29 | IPSL-CM5A-LR  | 30 | IPSL-CM5A-MR   |
| 31 | IPSL-CM5B-LR    | 32 | MIROC-ESM     | 33 | MIROC-ESM-CHEM |
| 34 | MIROC4h         | 35 | MIROC5        | 36 | MPI-ESM-LR     |
| 37 | MPI-ESM-MR      | 38 | MPI-ESM-P     | 39 | MRI-CGCM3      |
| 40 | MRI-ESM1        | 41 | NorESM1-M     | 42 | NorESM1-ME     |
| 43 | BCC_CSM1.1      | 44 | BCC_CSM1.1(m) | 45 | INM-CM4.0      |

- Several generations of coupled climate models have suffered from the presence of a double intertropical convergence zone (ITCZ) in the South Pacific throughout the year (Mechoso et al. 1995; Lin 2007; Li and Xie 2014; Adam et al. 2016, 2018) including in the most recent CMIP6 models (Tian and Dong 2020). In reality, an ITCZ does not occur in the South Pacific except in March and April (Hubert et al. 1969; Zhang 2001). The severity of the double-ITCZ bias in coupled model integrations is tightly linked to biases in the atmosphere component of that same model when fed with fixed sea surface temperatures (Xiang et al. 2017). The severity of this bias has been related to a range of processes in atmospheric models, including cloud radiative effects in the SH midlatitudes by some studies (Li and Xie 2014; Hwang and Frierson 2013) though not all (Kay et al. 2016; Adam et al. 2018), the convection scheme (e.g., Zhang and Wang 2006), and the formulation of the surface wind stress (e.g., Luo et al. 2005). A poorly simulated ITCZ (and associated Pacific cold tongue) in the mean state limit the confidence that can be placed in future projections of, for example, El Niño–Southern Oscillation (ENSO) and its teleconnections (AchutaRao and Sperber 2006; Bellenger et al. 2014; Li et al. 2016; Bayr et al. 2019, among others) if the projected changes depend on the mean state (He and Soden 2016).
  - The Agulhas Current forms in the Mozambique Channel and transports heat poleward off the South African coast (Lutjeharms 2007). Beyond the southern tip of the Agulhas Bank off the southern coast of South Africa, the Agulhas Current retroflects, with most of its waters feeding the south Indian subtropical gyre in the Agulhas Return Current. About 10%–20% of the current leaks westward into the adjacent South Atlantic (referred to as Agulhas Leakage), largely via rings and eddies with a characteristic spatial scale of around 100 km (Lutjeharms 2007). The Agulhas Return Current extends from the Agulhas retroflexion (~20°E) as far as 75°E, and its passage east remains largely zonal. Climate models with a coarsely resolved ocean (i.e., most models participating in CMIP) struggle to capture the ocean dynamics behind the retroflexion and leakage (Kwon et al. 2010; Holton et al. 2017). For example, models simulate too much leakage compared to observations by up to a factor of 3, and a concomitant reduction in retroflexion, even if the strength of the Agulhas Current itself is accurately simulated (Weijer et al. 2012). The sharp gradient in surface temperature between the Agulhas Return Current and colder waters farther poleward has been shown to influence local storm-track activity in the lower troposphere (Inatsu and Hoskins 2004; Liu et al. 2007; Small et al. 2014; Yao et al. 2016), though the impacts on the broader-scale circulation are less clear. Sampe et al. (2010) find that when a zonally symmetric SST gradient of similar strength to that near the Agulhas Return Current is inserted in a zonally symmetric aquaplanet model, the jet shift poleward, a result we return to in section 5 of this study.
  - Most current climate models suffer from an equatorward bias in the position of the SH midlatitude jet as compared to observations (Wilcox et al. 2012; Swart and Fyfe 2012a; Bracegirdle et al. 2013) including some models with jet position 10° from that observed, though this bias is reduced in the more recent Chemistry–Climate Model Initiative models (Son et al. 2018) and in CMIP6 (Curtis et al. 2020). The magnitude of the simulated surface response to increased greenhouse gases and the ozone hole may depend on the severity of this bias, with models that exhibit a more equatorward climatological jet bias also showing a larger poleward shift of the jet in response to ozone depletion or greenhouse gases (Kidston and Gerber 2010; Garfinkel et al. 2013b; Sigmond and Fyfe 2014, among others), though such a relationship does not appear to be evident in the CCMi simulations (Son et al. 2018), in the ozone-only forced simulations presented by Seviour et al. (2017), or in austral summer in CMIP5 models (Simpson and Polvani 2016). Such a bias is also associated with incorrect surface wind stress on the Southern Ocean, and hence with a biased Southern Ocean circulation (Swart and Fyfe 2012a,b). Some studies have suggested that such a bias is in part due to biases in cloud distribution (Ceppi et al. 2012), though the full range of causes is still unclear.
- This study aims to link these various biases together. In section 2 we demonstrate that poorly simulated SH stationary waves are related to a double ITCZ and a too-weak surface

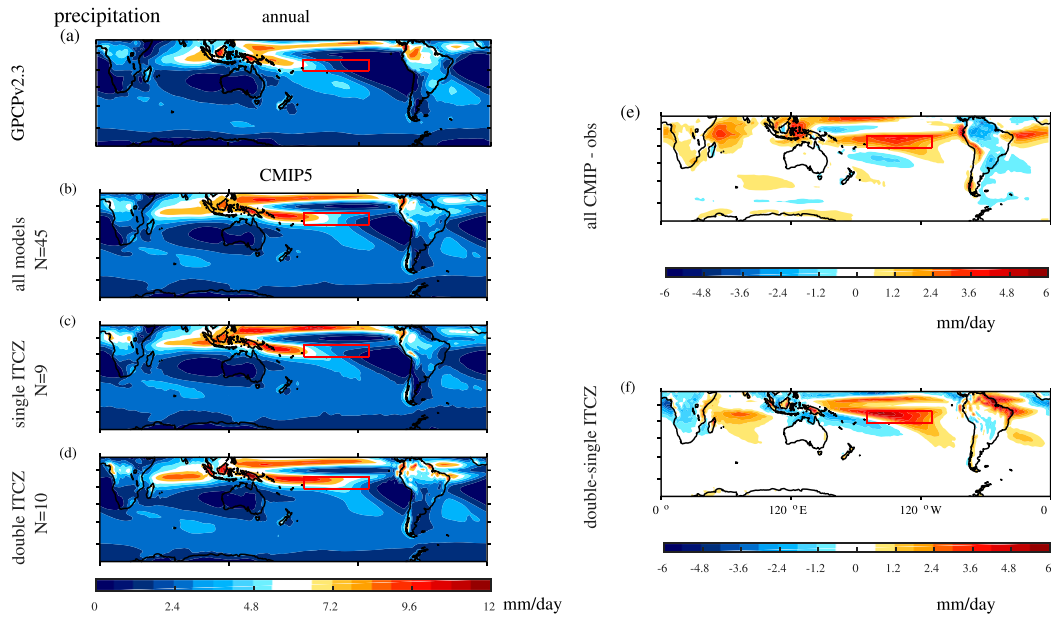


FIG. 2. As in Fig. 1, but for precipitation in GPCP ( $\text{mm day}^{-1}$ ). The contour interval is  $1.2 \text{ mm day}^{-1}$  for (a)–(d) and  $0.6 \text{ mm day}^{-1}$  for (e) and (f).

temperature gradient near the Agulhas in CMIP models. To better establish the causality of this relationship, we have developed an idealized GCM of relevance to the SH atmospheric circulation, and we introduce this model and discuss key sensitivities in section 3. We use integrations of this GCM to show that a double ITCZ is associated with a wave train pattern that degrades SH stationary waves (section 4). Finally, we use this same idealized GCM to show that a poorly represented Agulhas Return Current leads to an overly equatorward jet latitude and too-weak stationary waves (section 5).

## 2. Factors influencing the simulation of SH extratropical stationary waves in the CMIP5

We begin by considering the relationship between SH extratropical stationary waves and other biases in comprehensive climate models. We focus on 45 models that participated in CMIP5 (Taylor et al. 2012) listed in Table 1.

### a. Association between biased SH stationary waves and a double ITCZ

The observed precipitation climatology from 1979 through 2016 from the Global Precipitation Climatology Project (GPCP), version 2.3 (Adler et al. 2003), is in Fig. 2a, and the corresponding multimodel mean precipitation over the period 1985–2004 in the historical simulation is shown in Fig. 2b. The multimodel mean is characterized by too much precipitation in the tropical South Pacific (see the boxed region) as compared to that observed. Precipitation is larger than observed in all but two models (MIROC-ESM and MIROC-ESM-CHEM).

While this bias appears in nearly all models, its severity varies considerably. Figure 2c shows the precipitation climatology in models whose precipitation in the boxed region is between 100% and 175% of that observed (the MIROC models will be discussed later), while Fig. 2d shows the

precipitation climatology in models whose precipitation in the boxed region is more than 250% of that observed. By construction, precipitation is larger in the tropical South Pacific in Fig. 2d than in Fig. 2c, as quantified in Fig. 2e.

The corresponding stationary waves, defined here as the deviation of the time-averaged geopotential height at 300 hPa from its zonal average, is shown in Fig. 1. The amplitude of the stationary waves in the multimodel mean is weaker than that observed (Fig. 1a vs Fig. 1b), and the bias is most pronounced south of Africa and New Zealand (Fig. 1e). These biases south of Africa and New Zealand are more pronounced in models with a double ITCZ (Fig. 1d) as compared to those with a single ITCZ (Fig. 1c). The difference between the models with a double ITCZ and single ITCZ is shown in Fig. 1f, and is characterized by a wave-3 pattern in midlatitudes (Fig. 1e) with a relative ridge south of Australia and a trough southeast of New Zealand in models with a double ITCZ. This wave train may be associated with changes in the zonal distribution of rainfall in the tropical South Pacific.<sup>1</sup>

The relationship between the double ITCZ and biased stationary waves is summarized in Fig. 3. For each model, the climatological precipitation in the boxed region on Fig. 2 is compared to the difference in geopotential height between the red box and blue box on Fig. 1, with the red box representative

<sup>1</sup> Note that the difference in stationary waves between the multimodel mean and reanalysis does not resemble the difference in stationary waves between the single-ITCZ models and the double-ITCZ models. The corresponding differences in precipitation also differ from each other in the west Pacific and Maritime Continent (Figs. 2e,f). The possibility that precipitation in the Maritime Continent is important for the difference in stationary waves responses will be considered in section 4.

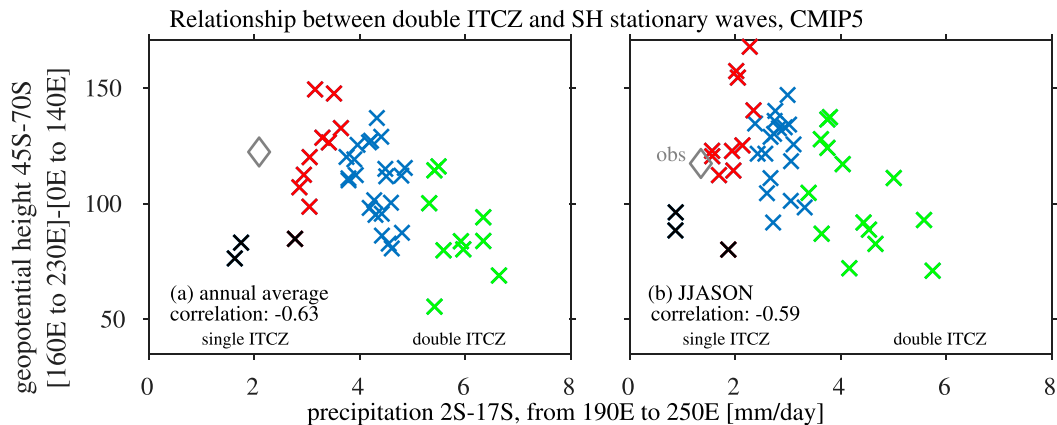


FIG. 3. Relationship between SH 300-hPa geopotential height zonal asymmetries and precipitation in the double-ITCZ region ( $17^{\circ}$ – $2^{\circ}$ S,  $190^{\circ}$ – $250^{\circ}$ E) in (a) the annual average and (b) June through November. The models included in Fig. 2c and Fig. 1c (e.g., less-pronounced double-ITCZ models) are shown in red, while the models included in Fig. 2d and Fig. 1d (e.g., severe double-ITCZ models) are shown in green. Observations (GPCP precipitation and ERA5 heights) are shown with a diamond, and models are shown with an x. Models with precipitation between 175% and 250% of that observed are in blue, and the MIROC models are in black.

of the wave-1 ridge and the blue box representative of the wave-1 trough. The models included in Fig. 2c and Fig. 1c (less pronounced double-ITCZ models) are shown in red, while the models included in Fig. 2d and Fig. 1d (severe double-ITCZ models) are shown in green. The MIROC models are shown with a black x, and observations (GPCP precipitation and ERA5 heights) are shown with a gray diamond. The relationship between the double ITCZ and stationary waves is significant at the 5% confidence level using a two-tailed Student's  $t$  test: models with a better simulated precipitation climatology in the SH tropics simulate more realistic stationary waves, and more than 35% of the variance in stationary waves is accounted for by the double ITCZ. The MIROC models are an exception to this general relationship, and these models are addressed in the discussion. The correlation is robust to variations of the spatial range of the red and blue boxes of  $\sim 20\%$  (not shown). A similar correspondence is evident both in the annual mean and in the June through November seasonal mean, the season when stationary waves are strongest.

#### b. Relationship between biased SH stationary waves in CMIP5 and a weak Agulhas Return Current

The realism of SH stationary waves in CMIP5 models is also related to the quality of the representation of the Agulhas Current, and specifically, the tight meridional surface temperature gradient associated with the Agulhas Return Current. Figure 4a shows the meridional 2-m temperature gradient in ERA5 data in the annual average, and Fig. 4b is as in Fig. 4a but for the near surface air temperature (tas) in 45 CMIP5 models listed in Table 1. While the multimodel mean represents the sharp gradient reasonably well, there is a wide diversity among the models. The models with a meridional temperature gradient in the Agulhas Return Current region (the black-boxed region) at least as strong as that observed are composited, and the mean surface temperature gradient for these models is

shown in Fig. 4c. The surface temperature gradient for a corresponding composite of models with a surface temperature gradient in this region less than 90% of the observed value is shown in Fig. 4d. By construction, the models included in Fig. 4d do not capture a strong gradient in this region.<sup>2</sup>

The corresponding stationary wave field in 300-hPa geopotential height is shown in Fig. 5, with the top two rows repeated from Fig. 1. The stationary waves are stronger in those remodels with a realistic surface temperature gradient near the Agulhas, as compared to models without such a gradient. This relationship is summarized in Fig. 6. For each model, the climatological meridional surface temperature gradient in the boxed region on Fig. 4 is compared to the difference in geopotential height between the red box and blue box on Fig. 5, with the red box representative of the wave-1 ridge and the blue box representative of the wave-1 trough. The models included in Fig. 4c and Fig. 5c (stronger meridional gradient models) are shown in red, while the models included in Fig. 4d and Fig. 5d (overly diffuse Agulhas) are shown in green. The relationship between the strength of the surface temperature gradient and the amplitude of the stationary waves is significant at the 5% confidence level using a two-tailed Student's  $t$  test: models with a better simulated surface midlatitude temperature gradient in the Agulhas Return Current region simulate more realistic stationary waves. The correlation is robust to variations of the spatial range of the red and blue boxes of  $\sim 20\%$  (not shown). A similar correspondence is evident both in the annual mean and in June through November.

<sup>2</sup> We find no relationship between the magnitude of the biased double ITCZ and the magnitude of the meridional surface temperature gradient near the Agulhas Return Current: the correlation of these in these 45 models is 0.04.

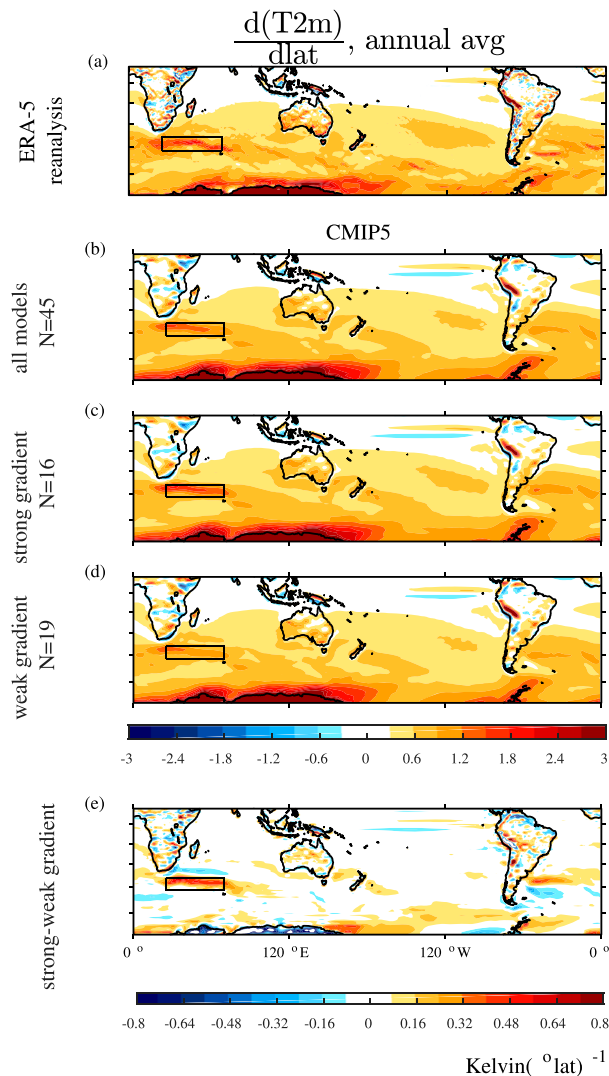


FIG. 4. (a) Climatology of the meridional 2-m temperature gradient in ERA5 data in the annual average. (b) As in (a), but in the 45 CMIP5 listed in Table 1; (c) as in (b), but in models with a surface temperature gradient in the Agulhas retroreflection region (the black-boxed region) at least as strong as that observed; (d) as in (b), but in models with a surface temperature gradient in this region less than 90% of the observed value; and (e) difference between (c) and (d). The contour interval is 0.3 K per degree latitude for (a)–(d) and 0.08 K per degree latitude for (e).

### 3. Toward a reasonable Southern Hemisphere circulation in an idealized model

While the results in section 2 indicate a statistically significant relationship between biased stationary waves and both a double ITCZ and a too-weak meridional SST gradient associated with the Agulhas Return Current, the causality of this connection is unclear. For example, Figs. 2c and 2d differ not just in the tropical South Pacific, and Figs. 4c and 4d differ not just near South Africa. Hence it is unclear how much of the stationary wave response is associated with the altered precipitation pattern in the tropical South Pacific and surface

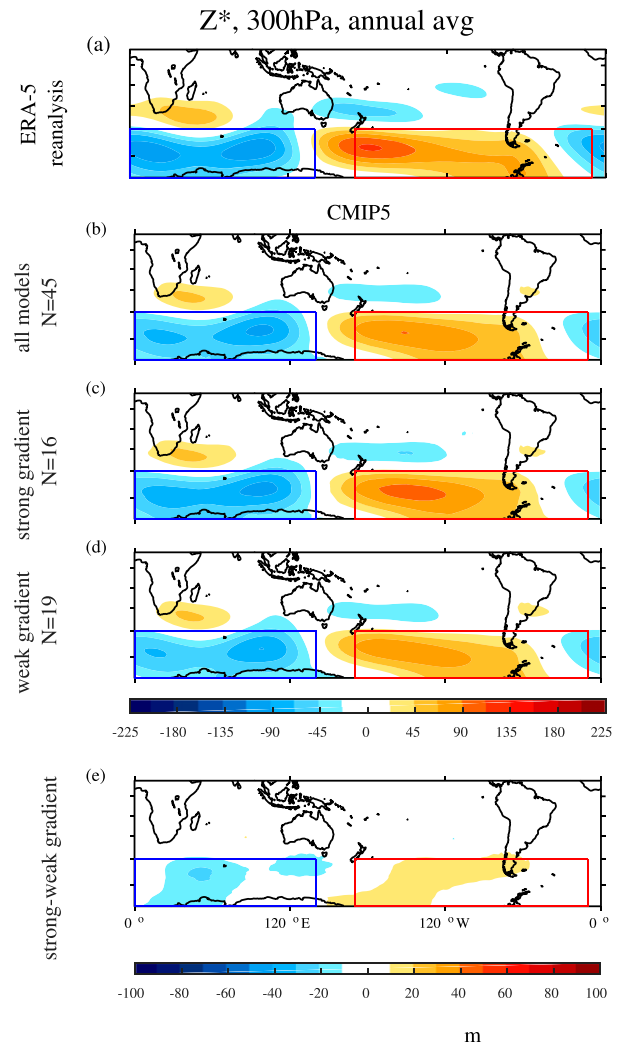


FIG. 5. As in Fig. 4, but for geopotential height at 300 hPa. The contour interval is 22.5 m for (a)–(d) and 10 m for (e).

temperature pattern south of Africa. To investigate the causality of this relationship, we have developed a simplified general circulation model that represents the Southern Hemisphere stationary waves and jet in order to understand their connections to SST biases in comprehensive climate models.

We begin with the model of an idealized moist atmosphere (MiMA) introduced by Jucker and Gerber (2017) and Garfinkel et al. (2020b). This model builds on the aquaplanet model of Frierson et al. (2006, 2007) and Merlis et al. (2013). Very briefly, the model solves the moist primitive equations on the sphere, employing a simplified Betts–Miller convection scheme (Betts 1986; Betts and Miller 1986), idealized boundary layer scheme based on Monin–Obukhov similarity theory, a slab ocean, the Rapid Radiative Transfer Model (RRTMG) radiation scheme (Mlawer et al. 1997; Iacono et al. 2000), and gravity waves following Alexander and Dunkerton (1999) and Cohen et al. (2013). Please see Jucker and Gerber (2017) for more details. Unless otherwise indicated, all simulations in this paper were

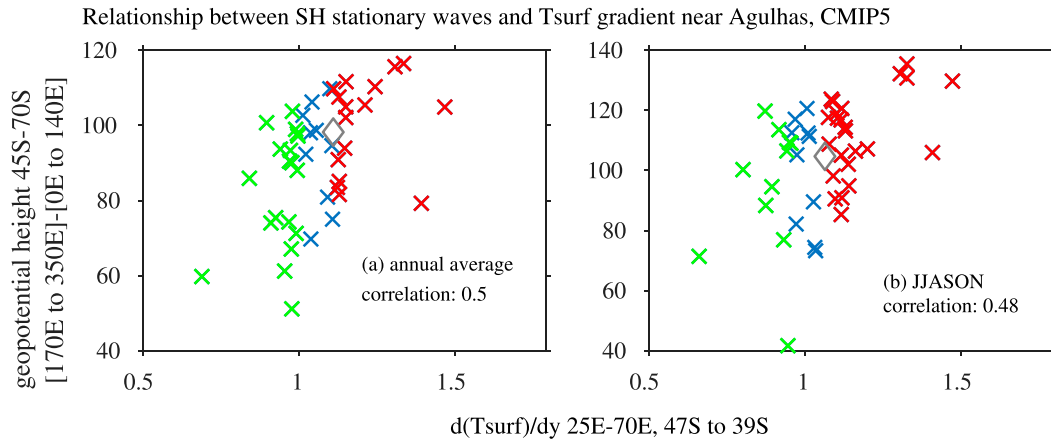


FIG. 6. Relationship between SH 300-hPa geopotential height zonal asymmetries and the meridional surface temperature gradient in the Agulhas retroreflection region (the black-boxed region on Fig. 4) in (a) the annual average and (b) June through November. The models included in Fig. 4c and Fig. 5c (e.g., gradient as strong as that observed) are shown in red, while the models included in Fig. 4d and Fig. 5d (too-weak Agulhas retroreflection) are shown in green. Other models are in blue. Reanalysis (ERA5) is shown with a diamond.

run with a triangular truncation at wavenumber 42 (T42; equivalent to a roughly  $2.8^\circ$  grid) with 40 vertical levels for 48 years, with the first 10 years treated as spinup. Globally averaged surface temperature changes after year 10 are less than 0.1 K.

Following Garfinkel et al. (2020b), we have added three sources of zonal asymmetry to the lower boundary of an initially zonally symmetric moist aquaplanet model: orography, ocean horizontal heat fluxes, and land–sea contrast (i.e., difference in heat capacity, surface friction, and moisture availability between oceans and continents). The specification of these forcings (especially the ocean horizontal heat fluxes) has been updated from Garfinkel et al. (2020b), and the updated analytic formulae are included in the appendix. The total ocean horizontal heat uptake is shown in Fig. 7a, and the 2-m temperatures in ERA5 reanalysis and of the slab ocean in the model are shown in Figs. 7b and 7c, respectively. We assess sensitivity to the representation of the Andes, which are smeared out at T42 resolution, below. This default model configuration is referred to as CONTROL in the rest of this paper.

The resulting stationary waves in CONTROL are shown in Fig. 8a. The SH stationary waves represent observed stationary waves as realistically as the multimodel mean of the CMIP5 and certainly better than the group of models with a double ITCZ south of Africa and southeast of New Zealand (Fig. 1d), though the entire pattern is shifted equatorward by  $\sim 5^\circ$  as compared to observations (Fig. 1a). The latitude of maximum winds at 820 hPa (i.e., jet latitude) in the control integration is  $50.4^\circ\text{S}$  in the annual average, which is better than that in most CMIP models (Wilcox et al. 2012; Swart and Fyfe 2012a; Bracegirdle et al. 2013): the average jet latitude in the 45 models considered here is  $49.2^\circ\text{S}$ . The observed surface wind maximum is near  $53^\circ\text{S}$  (e.g., Figs. 5–13 of Karpechko et al. 2018).

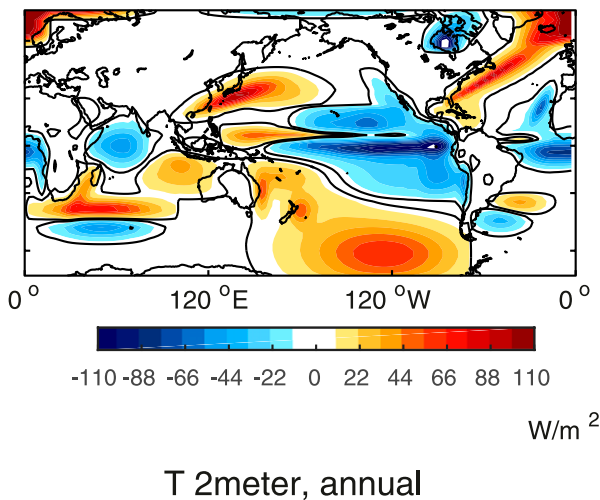
We find that the Northern Hemisphere stationary wave pattern is degraded under the configuration of ocean heat fluxes used here, when compared to the configuration of

Garfinkel et al. (2020b), when both are run at T42 resolution (not shown). However, an increase in resolution from T42 to T85 in the configuration used here leads to improved stationary waves in the Northern Hemisphere. Previous work has found that high resolution is needed in order to capture the full response to a narrow Gulf Stream and Kuroshio (Minobe et al. 2008; Xu et al. 2011; Small et al. 2014; Yao et al. 2016). The configuration of Garfinkel et al. (2020b) imposed broad regions of warming associated with the Gulf Stream and Kuroshio, and hence we suspect that the atmosphere could respond in a more realistic manner even at T42. In the rest of this paper we focus on the SH only.

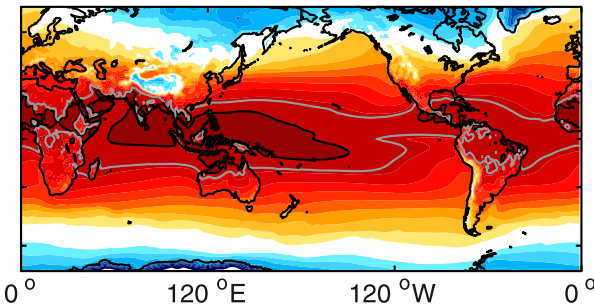
The importance of ocean horizontal heat fluxes for SH stationary waves is demonstrated in Fig. 8b, which shows the stationary waves that result if we include land–sea contrast and orography as in the control simulation, but without any zonally asymmetric ocean heat flux [we still apply a zonally uniform meridional ocean heat flux, Eq. (A4) in the appendix]. The SH stationary waves are significantly weaker, and the degradation of the ridge near New Zealand is particularly acute. Hence, the comparison of Figs. 8a and 8b illustrates how crucial zonal ocean heat fluxes are to the SH climatology.

The degradation in SH stationary waves when east–west ocean heat fluxes are excluded in Fig. 8b is associated with overly zonal precipitation in the deep tropics. Figure 9 shows the climatology of precipitation in CONTROL and in the simulation in which east–west ocean heat fluxes are excluded. While the simulation of the land precipitation is qualitatively similar (including the Indian monsoon, not shown) compared to that in the control simulation when east–west ocean heat fluxes are excluded (bottom of Fig. 9), precipitation in the deep tropics is not enhanced in the far west Pacific relative to the east, and Indian Ocean precipitation is also too zonal. This result suggests that midlatitude SH stationary waves are very sensitive to the zonal structure of precipitation in the tropics.

## (a) ocean heat uptake, CONTROL



## (b) ERA5



## (c) CONTROL

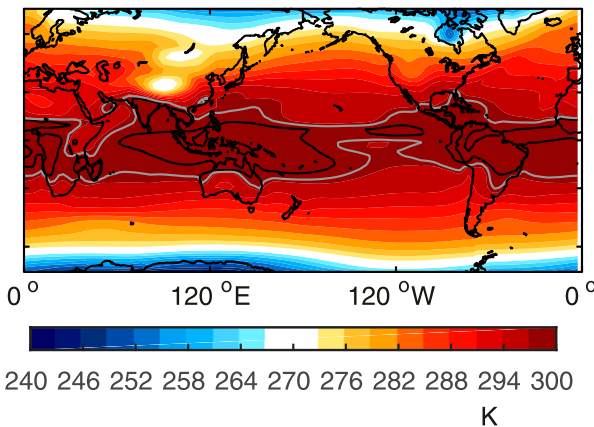


FIG. 7. (a) Ocean heat uptake ( $\text{W m}^{-2}$ ) in CONTROL. Two reanalysis/satellite-based estimate of ocean heat flux can be found in Forget and Ferreira (2019) and Trenberth et al. (2019). Climatology of (b) 2-m temperature in ERA5 data and (c) of the slab ocean (i.e., surface temperature) in the CONTROL integration in the annual average, with the 298- and 300-K isotherms in gray and black.

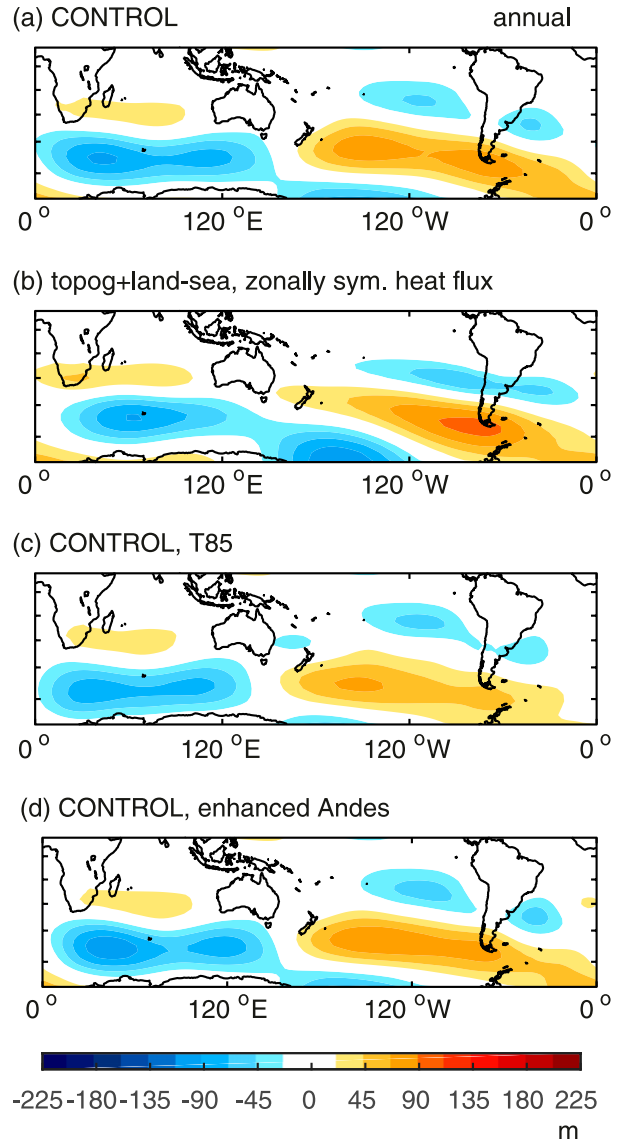
 $Z^*$ , 300hPa

FIG. 8. Zonally asymmetric component of geopotential height at 300 hPa in the annual average (a) in the control integration as detailed in the appendix and (b) in an integration with topography and land-sea contrast as in control but with ocean heat fluxes as specified by Eq. (A4) only; (c) as in (a), but at T85; (d) as in (a), but with the Andes enhanced as described in the text. The contour interval is 22.5 m.

The stationary waves when the model is run at double the resolution (T85 truncation) are shown in Fig. 8c. The stationary waves are similar at T42 and T85, though there are two notable differences: the stationary waves are somewhat weaker and shifted poleward at T85. The latitude of the lower-tropospheric zonal wind maximum (i.e., the extratropical jet) is also shifted poleward by  $\sim 0.6^\circ$  at T85. The higher-resolution integration better captures the sharp transition from a ridge to a trough downstream of South America (Fig. 8a vs Fig. 8c), possibly due to its ability to better resolve the Andes. In summary, the

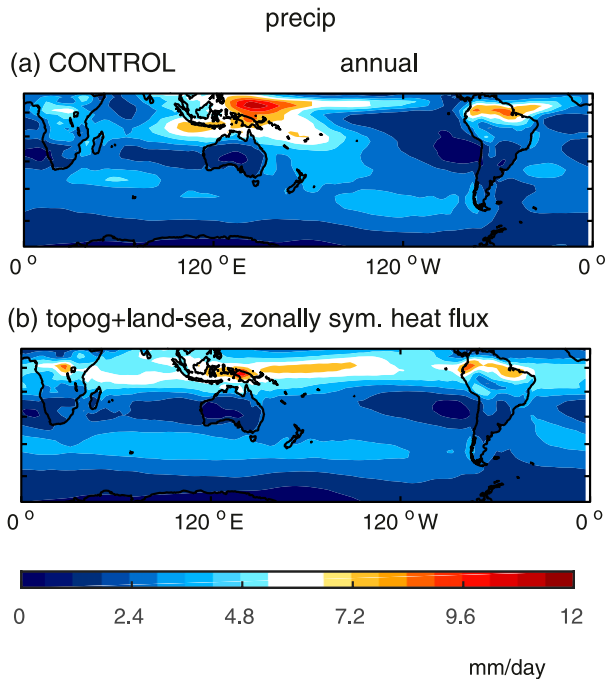


FIG. 9. As in Figs. 8a and 8b, but for precipitation. The contour interval is  $1.2 \text{ mm day}^{-1}$ .

structure of the stationary waves is improved at T85 as compared to T42, though the amplitude is not. Given the overall similarity of the T42 and T85 integrations, we focus on lower-resolution integrations for the remainder of the study.

Observed topography is used for the most realistic experiment, albeit at the resolution of the model with no effort to adjust the amplitude to preserve ridge heights (sometimes referred to as envelope topography), but with regularization as in Lindberg and Broccoli (1996). We set the “ocean topog smoothing” parameter of this scheme to 0.995 to minimize Gibbs ripples over the Himalayas and Andes. The T42 resolution smears out the Andes, and it is conceivable that this would degrade the stationary waves. Figure 8d assesses sensitivity to the effective ridge height of the Andes. Before the regularization procedure is performed, we first multiply the observed topography in the region  $6^{\circ}\text{--}63^{\circ}\text{S}$ ,  $230^{\circ}\text{--}300^{\circ}\text{E}$  by a factor of 1.75. The net effect is that after topography regularization is completed the maximum ridge heights are similar to the maximum gridscale ridge heights from observations. The stationary waves in Fig. 8a and in Fig. 8d are nearly indistinguishable. Thus, the representation of the Andes has little effect on the large-scale stationary waves. This lack of sensitivity appears to be consistent with that found by Takahashi and Battisti (2007, see their Fig. 6), who find that the remote effect of the Andes saturates for realistic topographic heights.

#### 4. Impact of a double ITCZ

We now use the idealized model introduced in section 3 to understand the impact of biases in tropical SSTs and precipitation (i.e., a double ITCZ) on extratropical stationary waves. Figure 7 shows the surface temperatures in CONTROL and observed, and

while the idealized model represents the large-scale pattern of surface temperatures, biases are present in, for example, the tropical South Pacific. Our approach is to add heat fluxes to the ocean to reduce (or accentuate) SST biases, and hence improve (or degrade) tropical precipitation. We can then understand how the extratropical atmosphere responds to these changes in the tropics. To do this, we will consider two different perturbations: one focused on meridional heat transport and the second focused on zonal heat transport. These two strategies allow us to assess the robustness of our approach, and also assess sensitivity to how changes in Maritime Continent precipitation evident in the CMIP5 intermodel difference (Fig. 2f) influence stationary waves.

We first “impose” a double ITCZ by modifying the meridional heat fluxes of the slab ocean in the tropical Southern Hemisphere (Fig. 10a), comparing to an analogous simulation in which the ocean heat flux perturbation is of opposite sign (Fig. 10b) in order to improve the signal-to-noise ratio. The functional form for the perturbation is included in the appendix. In both cases no net heating is added. Rather, the ocean heat flux in CONTROL is simply redistributed, ensuring similar globally averaged temperatures. When extra heat is fluxed out of the tropical southeast Pacific and into the extratropical Pacific (Fig. 10b), the region of cold tropical SSTs and reduced precipitation is larger as compared to a simulation with less flux of heat out of the tropical South Pacific (Figs. 10d,f vs Figs. 10c,e). Associated with this imposition of a double ITCZ is strengthened divergence at 300 hPa in the tropical southeast Pacific (boxed region on Fig. 10g as compared to Fig. 10h), coupled with reduced divergence over the South Pacific convergence zone (SPCZ) region farther west. This dipole in divergence weakens the Rossby wave source dipole [computed as in Sardeshmukh and Hoskins (1988), using daily data] in the tropical South Pacific in the double-ITCZ integration (Fig. 10i), compared to the integration with a single ITCZ (Fig. 10j).

The net effect on stationary waves is shown in Fig. 11. SH stationary waves are stronger in the simulation with a single ITCZ (Fig. 11b), and more closely resemble those observed (Fig. 11e). The difference in the stationary waves between the two simulations is shown in the right column of Fig. 11, and the stationary wave pattern is weakened south of Africa and near New Zealand in response to a double ITCZ. In addition to the subtropical changes, there is a deeper trough near  $120^{\circ}\text{W}$  in the subtropics for a single ITCZ, which is related directly to the lack of subtropical precipitation farther equatorward and changes in upper-level divergence and the Rossby wave source. This change in the trough near  $120^{\circ}\text{W}$  in the subtropics initiates a poleward propagating Rossby wave train that appears to encompass most of the extratropics (right column of Fig. 11).

We next assess the sensitivity of the stationary waves to the pattern of the SSTs, by alternately “imposing” a double ITCZ in a second experiment in which heat fluxed out of the tropical east Pacific is redistributed to the tropical west Pacific. We again compare to a parallel integration in which the ocean heat flux perturbation is imposed with the same pattern but opposite sign. The difference in ocean heat uptake for the pair of integrations (double–single) is shown in Fig. 12a: there is a strong zonal dipole in heat uptake in the Pacific, which either

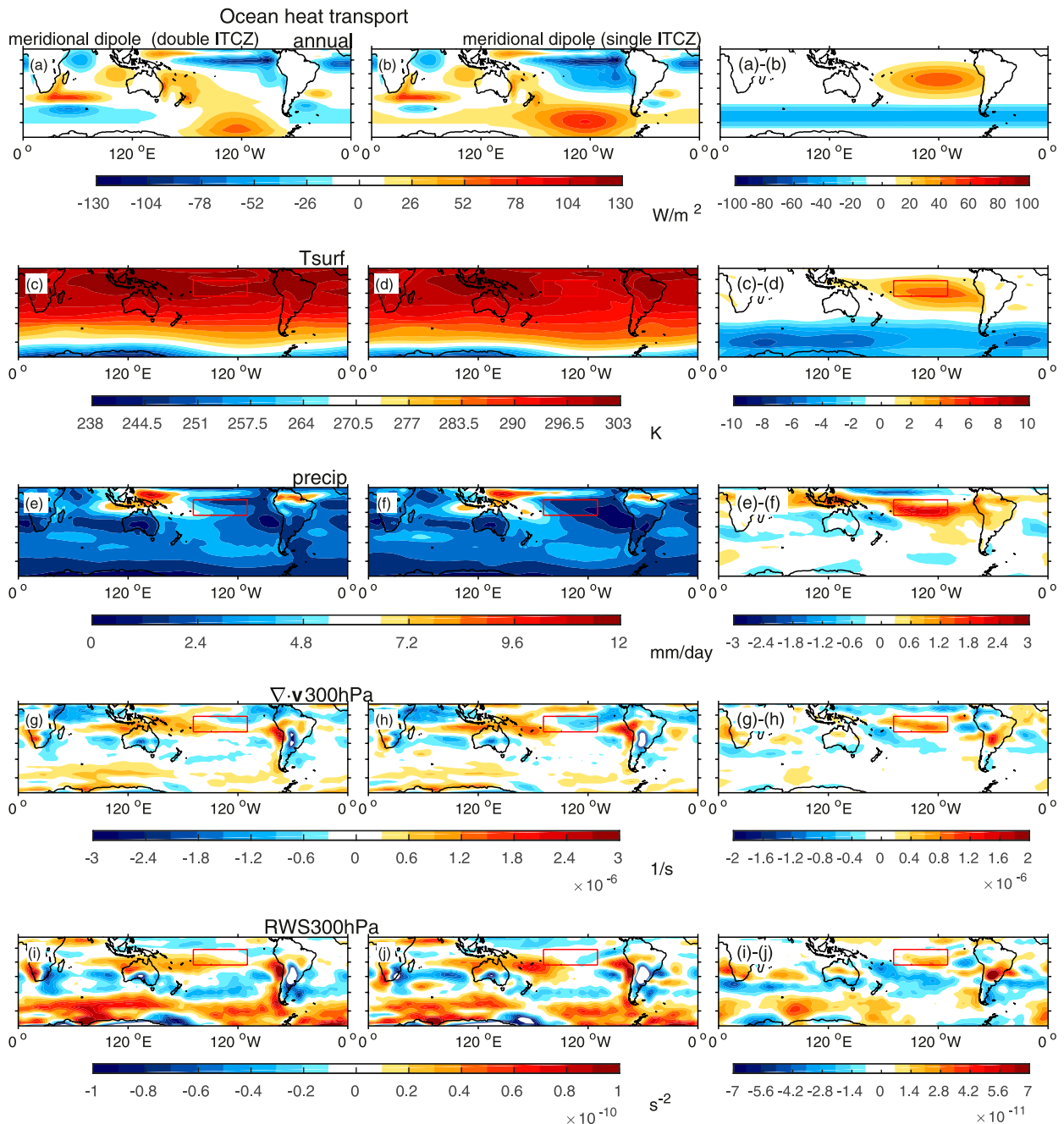


FIG. 10. Annual averaged response to a (left) double ITCZ vs a (center) single ITCZ, and the (right) difference between the two, with a meridional dipole in the South Pacific allowing or restricting a double ITCZ. (a),(b) ocean heat flux; (c),(d) surface temperature; (e),(f) precipitation; (g),(h) divergence of the 300-hPa wind; and (i),(j) Rossby wave source at 300 hPa.

eliminates the climatological zonal dipole or accentuates it. As before no net heating is added.

A zonal dipole in ocean heat uptake leads to a similar dipole in surface temperature distribution (Fig. 12b), and also to a similarly structured precipitation anomaly with either a South Pacific convergence zone or a double ITCZ (Fig. 12c). Changes in tropical divergence in the tropical South Pacific (Fig. 12d) resemble those in Figs. 10g and 10h: a zonally oriented dipole is

stronger for the single-ITCZ cases in Fig. 12d than for the double-ITCZ case. Consistent with this, the zonal dipole in Rossby wave source in the South Pacific is stronger for a single ITCZ (Fig. 12e). This difference in tropical precipitation affects SH stationary waves (Figs. 11c,d). The amplitude of the SH stationary waves increases when the double-ITCZ bias is eliminated, leading to a closer correspondence with observations (Fig. 11e).

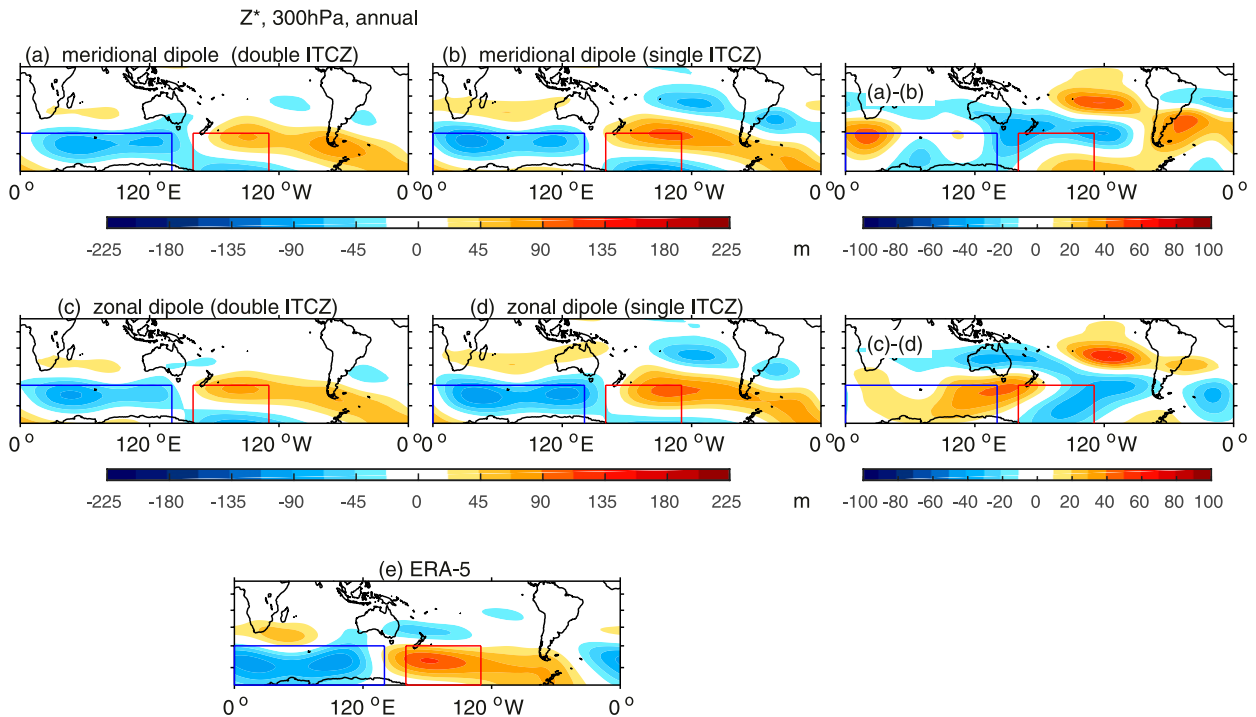


FIG. 11. As in Figs. 10a and 10b, but for the zonally asymmetric component of the geopotential height at 300 hPa; (a),(b) meridional dipole in the South Pacific so as to allow or restrict a double ITCZ; (c),(d) zonal dipole in the South Pacific; and (e) ERA5 reanalysis data (repeated from Figs. 1a and 5a).

The difference in the stationary waves between the two zonal dipole simulations can be compared to the difference for a meridional dipole (Figs. 11a,b) and for CMIP data (Figs. 1e,f). There are certain features common to Figs. 1e and 1f and the difference plots in the right column of Fig. 11: a ridge in the subtropical Pacific near 120°W and a trough farther poleward, and also a ridge south of Africa. These common features therefore are apparently a robust response to a double ITCZ, though the specifics of how the ridge south of Africa develops likely differs among the idealized model experiments and CMIP. The extratropical trough near 120°W and the ridge south of Africa associated with a double ITCZ weakens the stationary wave pattern in both CMIP and in the idealized model. The overall effect is that spurious local Rossby wave source, which generates a wave train into the South Pacific that is out of phase with the climatological stationary wave pattern leading to destructive interference and a too-weak amplitude.

In other regions, however, the responses to a meridional and zonal dipole in the idealized model differ, but these differences are likely related to the precipitation outside of the double-ITCZ region (e.g., in the west Pacific and Maritime Continent). The precipitation response for a meridional dipole (Figs. 10e,f) resembles the difference between the CMIP multimodel mean and reanalysis (Fig. 2e): precipitation is enhanced not only in the double-ITCZ region, but also throughout much of the deep tropics south of the equator. Consistent with this, both a meridional dipole forcing and the CMIP minus reanalysis

difference feature a similar stationary wave response (Figs. 1e and 11a,b), though as mentioned earlier the stationary wave pattern in the idealized model is shifted  $\sim 5^\circ$  equatorward of that in CMIP and observations.

The precipitation response for a zonal dipole (Fig. 12c) resembles the difference between the CMIP double-ITCZ and single-ITCZ models (Fig. 2f): precipitation is enhanced in the double ITCZ region but reduced over the Maritime Continent. Consistent with this, both a zonal dipole and the CMIP inter-model difference feature a similar stationary wave response (Figs. 1f and 11c,d) throughout the extratropics, with the only exception the Indian Ocean.

The changes in stationary waves associated with the ITCZ also affect the stratosphere. Namely, the double-ITCZ change is associated with a stronger stratospheric polar vortex ( $\sim 7 \text{ m s}^{-1}$  increase in zonal winds at 10 hPa, 60°S in the winter season June through August) as compared to the simulations with a single ITCZ. This difference is associated with a weaker wave-1 stationary wave pattern, which leads to a reduction in wave-1 heat flux (a proxy for vertical wave propagation) at 50°S and 250 hPa by 40%. Many comprehensive models suffer from a too-strong vortex. This work suggests the importance of tropical precipitation for the entire stratosphere–troposphere system.

### 5. Impact of an overly diffuse Agulhas Current

We now consider the connection between SST biases in the Agulhas region, and specifically a weakened meridional

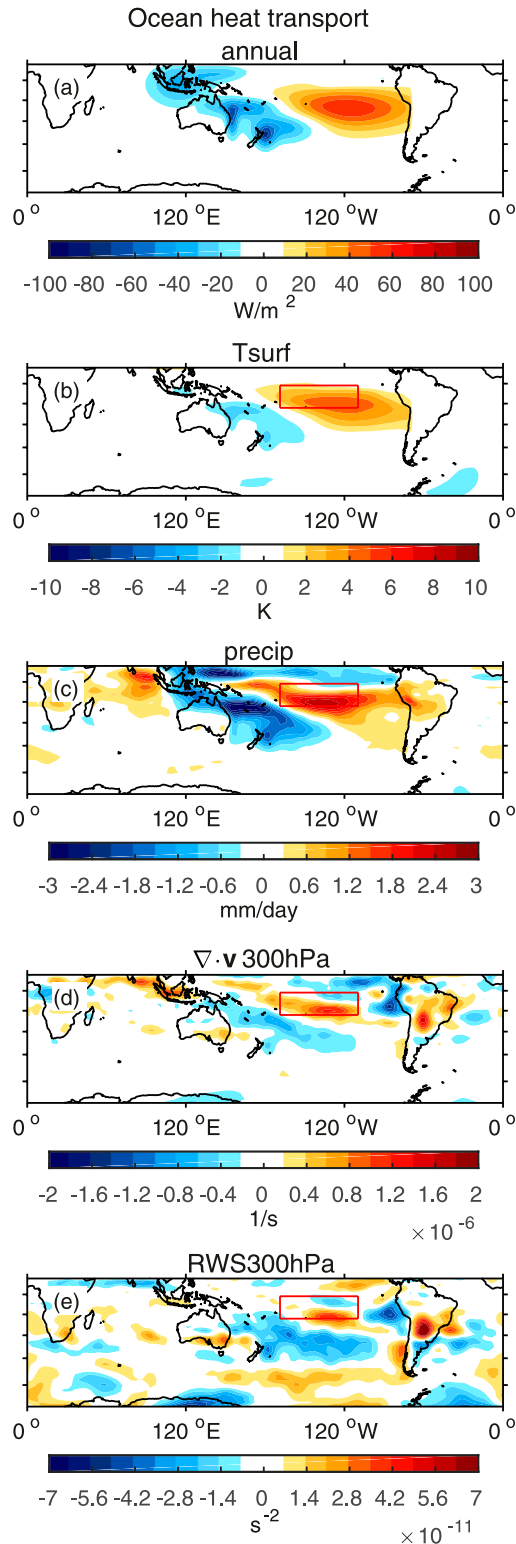


FIG. 12. As in the right column of Fig. 10 but for the experiments with a zonal dipole in the South Pacific so as to allow or restrict a double ITCZ.

temperature gradient off the coast of Africa associated with a diffuse Agulhas Return Current, and biases in the simulation of the extratropical jet and stationary waves in the SH. We modify the SSTs in the Agulhas region as shown in Figs. 13a and 13b. In Fig. 13a, the zonally localized SST gradient associated with the Agulhas is enhanced as compared to CONTROL, while in Fig. 13b the zonally localized SST gradient is removed. As before, no net heating is added, rather the ocean heat flux in CONTROL is redistributed to approximate the impact of Agulhas Current retroflexion. The functional form of the ocean heat flux perturbation is given in Eq. (A7) in the appendix. By construction, the surface temperature meridional gradient is stronger in Fig. 13c as compared to Fig. 13d.

A sharper surface temperature meridional gradient near the Agulhas leads to changes in stationary waves. Figure 14a shows the stationary wave pattern in the simulation with enhanced regional structure, while Fig. 14b shows the stationary wave pattern when regional structure associated with the Agulhas is removed. The stationary wave pattern is both stronger and located farther poleward in Fig. 14a and is more realistic than that shown in Fig. 14b except in the Atlantic sector where there is too strong of a ridge as compared to ERA5 (Fig. 14e). The pattern of changes in the stationary waves broadly resembles that seen in CMIP models in Fig. 5e in the Indian Ocean sector, indicating that the relationship seen in CMIP5 models in the Indian Ocean sector is indeed forced by the surface temperature gradient.

How does an enhanced surface temperature gradient in the Agulhas Return Current region lead to stronger stationary waves? We first consider and reject three hypotheses—Rossby wave source, changes in eddy activity, and changes in jet latitude—before focusing on the importance of the zonal structure of the upper-level temperature response to a zonally localized Agulhas perturbation. We begin with changes in precipitation in Figs. 13e and 13f. Local changes in precipitation appear as expected, with enhanced precipitation over the region that warms, and suppressed precipitation over the region that cools, in addition to precipitation changes elsewhere. Changes in the Rossby wave source resemble a dipole near the Agulhas region mimicking the precipitation dipole in this region in Figs. 13e and 13f (not shown), and do not seem to be capable of explaining the behavior using the vorticity budget arguments of Honda et al. (1999), in which centers of action in height are located near nodes of the Rossby wave source.

Figures 13g and 13h show the transient kinetic energy in the lower troposphere,  $(u'^2 + v'^2)/2$ , where  $u'$  and  $v'$  are the high-pass-filtered zonal and meridional winds obtained by applying a fifth-order Butterworth filter with an 8-day cutoff. Consistent with Sampe et al. (2010), transient kinetic energy is increased in the presence of a stronger surface temperature gradient. A similar increase in transient kinetic energy aloft, and in eddy zonal momentum ( $u'v'$ ) and heat ( $v'T'$ ) flux by the meridional wind, also occurs in response to a tighter SST gradient [not shown; consistent with the energetic arguments of Mbengue and Schneider (2017)].

While it is tempting to naively conclude that enhanced eddy activity necessarily leads to stronger stationary waves, such an assumption is, in fact, incorrect. It is helpful to

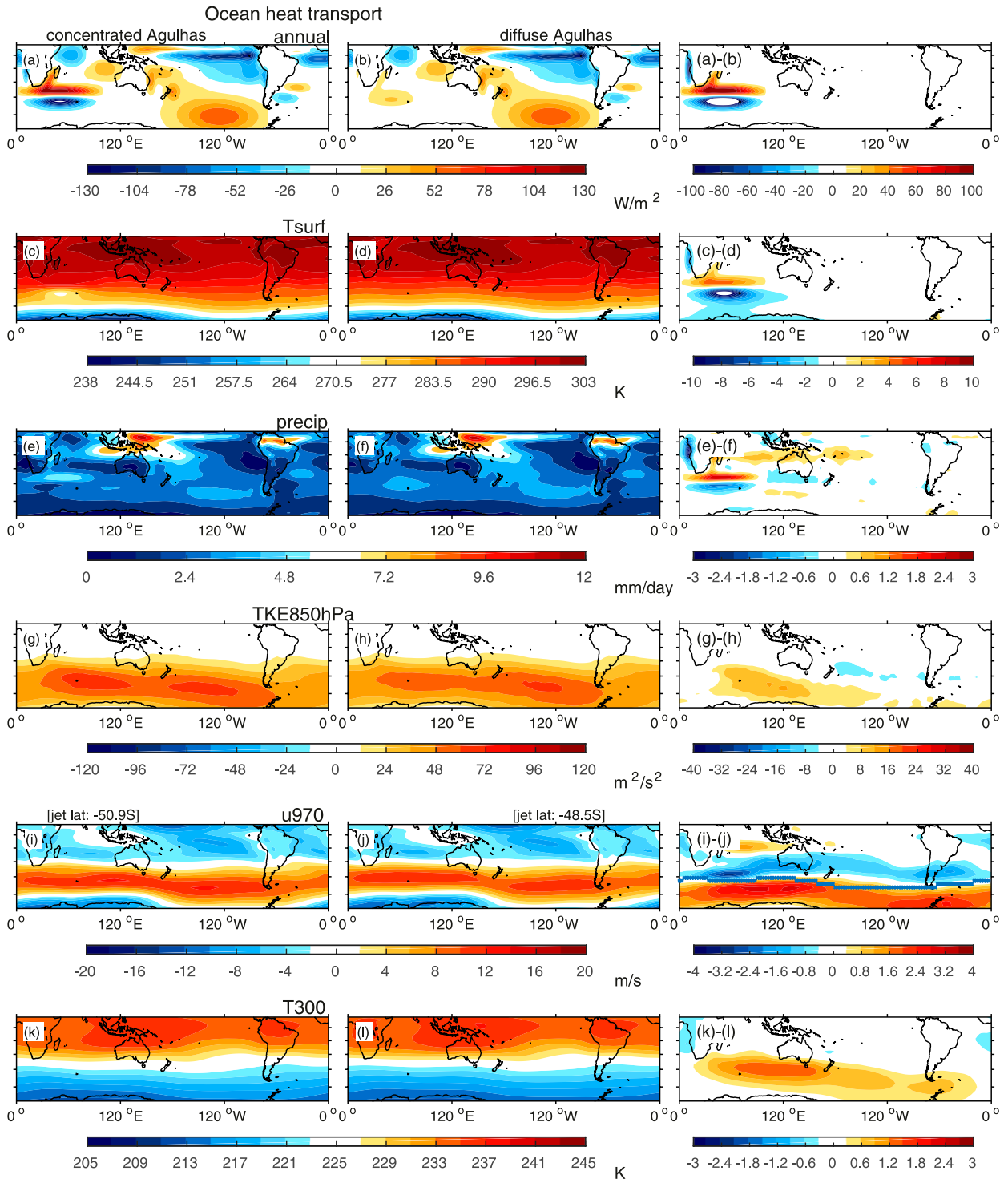


FIG. 13. (a)–(f) As in Fig. 10, but for a (left) sharp vs a (center) diffuse Agulhas Current system. (g),(h) Transient kinetic energy at 850 hPa; (i),(j) zonal wind at 970 hPa, with the climatological jet latitude indicated in the difference plot; and (k),(l) temperature at 300 hPa.

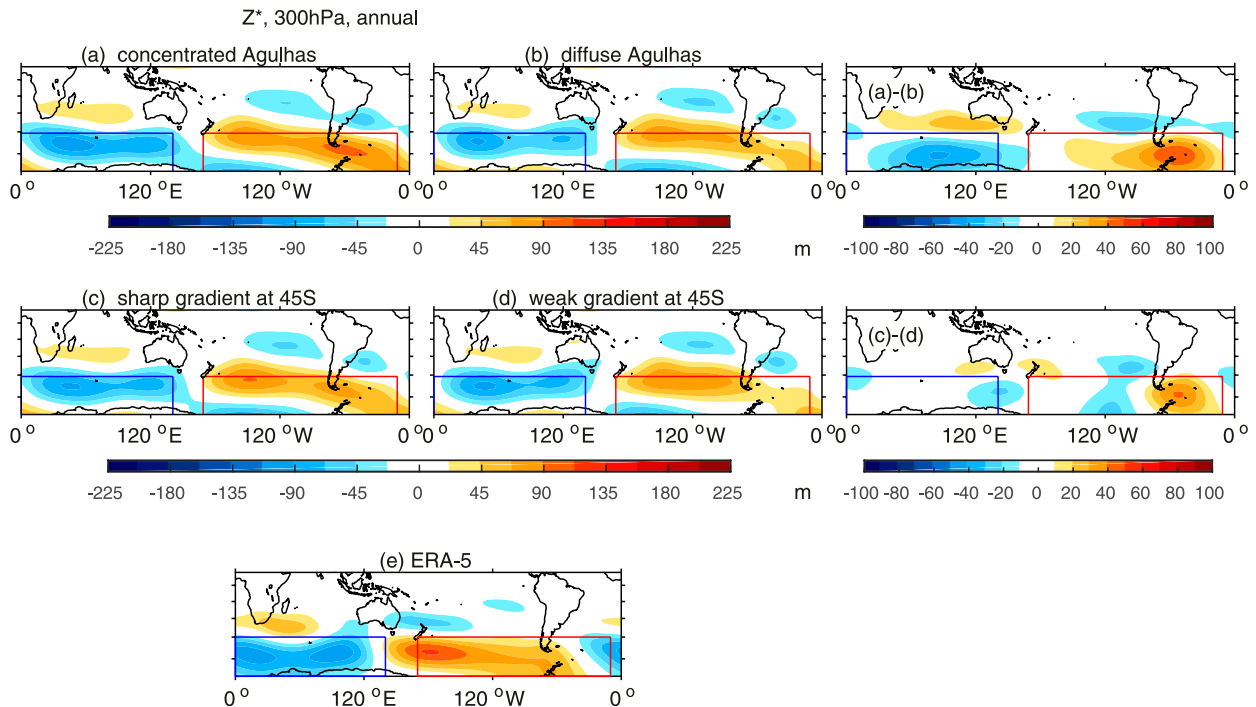


FIG. 14. As in Fig. 11, but for the experiments probing the impact of the meridional surface temperature gradient near the Agulhas on the zonally asymmetric component of the geopotential height at 300 hPa; (a),(b) zonally confined perturbation and (c),(d) zonally symmetric perturbation. (e) ERA5 reanalysis (repeated from Figs. 1a and 5a).

contrast the changes in stationary waves in response to an enhanced surface temperature gradient in the Agulhas Return Current region to changes in stationary waves when a zonally symmetric ocean heat flux perturbation at these same latitudes is applied. Figure 15a is similar to Figs. 13a and 13b, but the ocean heat flux perturbation is applied in a zonally symmetric manner [see Eq. (A8)]. This leads to surface temperature and precipitation perturbations that mimic those in Figs. 13c–f in the Agulhas region, except that they are zonally symmetric. It is clear from Fig. 15d that transient kinetic energy also increases, and in Figs. 13g, 13h, and 15d the strengthening of eddy activity extends over much of the extratropics. However, changes in stationary waves are weak for the zonally symmetric perturbation (Figs. 14c,d) and do not resemble those for a zonally confined perturbation (Figs. 14a,b) or in CMIP5 data. Hence, a zonally symmetric change does not yield the same stationary wave response even if eddy activity increases; that is, the confinement to the Agulhas region is particularly important.

The latitude of the jet maximum increases in response to a stronger surface meridional temperature gradient in the Agulhas Return Current region. Specifically, the surface jet is shifted more than  $3^\circ$  poleward if the regional structure of the Agulhas is included (Figs. 13i,j). Note, however, that there is no statistically significant relationship between jet latitude and the strength of the surface temperature meridional gradient in this region in CMIP5 models. Furthermore, the surface jet is shifted poleward by  $4^\circ$  if a zonally symmetric perturbation is included (Fig. 15e), yet changes

in stationary waves are weak in Figs. 14c and 14d and do not resemble those in Figs. 14a and 14b (except near South America, which we speculate may be due to changes in orographic generation of stationary waves from the Andes due to a change in jet latitude). Hence the stationary wave response to SSTs in the Agulhas Return Current region is not directly associated with the jet shift caused by these anomalous SSTs.

Thus far we have shown that the stationary wave response is not associated with the Rossby wave source, jet latitude, or changes in eddy activity. In contrast, the stationary wave response can be understood (in a diagnostic sense) using the thermodynamic budget of Wills and Schneider (2018) and Garfinkel et al. (2020b). The full details of the application of the zonally asymmetric temperature budget are included in the online supplemental material, and here we include only a brief overview for brevity. The thermodynamic budget relies on changes in temperature aloft, and hence we show changes in 300-hPa temperature in Figs. 13k, 13l, and 15f for a zonally confined and zonally symmetric perturbation, respectively. A local ocean heat flux perturbation near the Agulhas leads to local changes in upper-level temperature (Figs. 13k,l), while a zonally symmetric ocean heat flux perturbation leads to a zonally symmetric response of upper-level temperature (Fig. 15f). In both, in the same region in which transient eddy kinetic activity is increased, temperatures aloft also increase in midlatitudes. The full details of why are included in the supplemental material, but briefly recall that a stronger meridional surface temperature gradient also leads to enhanced

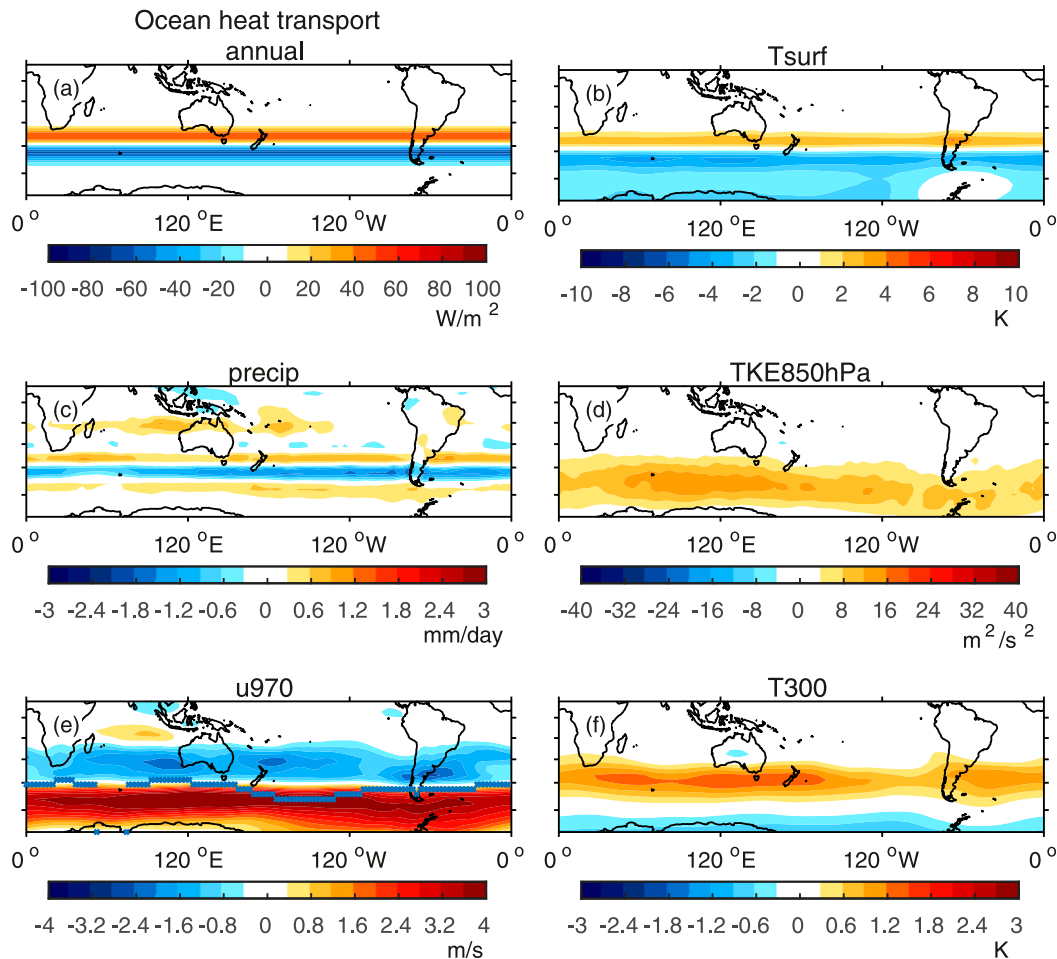


FIG. 15. As in the right column of Fig. 13, but for a zonally symmetric ocean heat flux perturbation at the same latitudes of the perturbation imposed for Fig. 13.

eddy heat ( $vT'$ ) flux by the meridional wind. A stronger heat flux should be expected to lead to warming of the midlatitudes while slightly cooling subtropical latitudes. While the increase in transient kinetic energy is present both for the zonally symmetric perturbation and also when the perturbation is confined to near the Agulhas, the increase in Figs. 15d and 15f is zonally symmetric and does not extend toward Africa.

This zonal structure of the upper-level temperature allows for a diagnostic interpretation of the stronger stationary waves in Figs. 14a and 14b as compared to Figs. 14c and 14d. Namely, only for a zonally confined perturbation does the Agulhas perturbation modify zonal advection of temperature, and hence lead to a change in meridional advection of temperature in order to maintain a steady state budget. A change in the meridional advection of temperature mandates a change in the meridional wind, and hence an altered stationary wave pattern, as discussed in detail in the supplemental material.

Overall, only a localized change in the Agulhas region gives similar stationary wave changes to that seen in CMIP5. A zonally symmetric change does not yield the same stationary wave response, that is, the Agulhas region is crucial.

## 6. Discussion and conclusions

Climate change projections differ among models, with across-model differences particularly pronounced at regional scales (Knutti and Sedláček 2013; He and Soden 2016; Garfinkel et al. 2020a). While some of this spread is likely due to internal variability in the climate system, and hence is irreducible, much of the spread may arise from model biases. Reducing these biases would allow us to reduce the uncertainty in future circulation trends. There is substantial evidence that an improved basic state climatology will improve regional climate projections (e.g., Held and Soden 2006; Matsueda and Palmer 2011; Scheff and Frierson 2012; Ogawa et al. 2015; He and Soden 2016). Here we considered processes that impact Southern Hemisphere stationary waves, focusing on the role of two systematic biases that appear in many CMIP models: a spurious intertropical convergence zone (ITCZ) in the South Pacific, and a too-weak sea surface temperature gradient in the Agulhas at the tip of South Africa.

A double ITCZ was shown to bias stationary waves in the midlatitude Southern Hemisphere. Specifically, spurious precipitation in the tropical South Pacific is associated with anomalous upper-tropospheric divergence and a Rossby wave source

that weakens the climatological zonal dipole in the South Pacific. This spurious Rossby wave source generates a wave train into the South Pacific that is out of phase with the existing stationary wave pattern in the Pacific sector. Specifically, the stationary wave pattern in response to a spurious double ITCZ includes a ridge south of Africa and trough near New Zealand, both of which destructively interfere with the stationary waves otherwise present. This relationship is evident both in CMIP5 integrations and in targeted experiments of an idealized atmospheric model.

Two versions of one CMIP5 model, MIROC-ESM and MIROC-ESM-CHEM, provide an exception to this relationship. They exhibit a single ITCZ, yet poorly represent SH stationary waves (see the black dots in Fig. 3). While these models exhibit a better climatological precipitation than any other CMIP5 model in the South Pacific, they suffer from too much precipitation in the Indian Ocean and an overly weak South Pacific convergence zone (Fig. 6cd of Watanabe et al. 2011). The net effect is that tropical precipitation is too zonal. The high biased precipitation in the Indian Ocean in particular is an outlier as compared to the other models we have examined and exceeds observed precipitation by a factor of 2. As is evident in Figs. 8b and 9b, an overly zonal climatology of tropical precipitation leads to biased stationary waves. Hence the too-weak stationary waves in this model can be associated with an overly zonal precipitation structure, despite its relative success in the east and central Pacific. Note that the high-resolution MIROC4h model has a more realistic tropical precipitation climatology in the Indian Ocean than the lower-resolution MIROC models, and consistent with this, has a reasonable stationary wave pattern.

In section 5, we showed that a diffuse Agulhas Return Current leads not only to biases in local precipitation and temperature, but also to changes in eddy activity throughout much of the extratropical Southern Hemisphere. A sharper surface temperature gradient in the Agulhas Return Current region leads to enhanced eddy activity (Inatsu and Hoskins 2004; Small et al. 2014; Yao et al. 2016) and a warming of midlatitudes and a cooling of the subtropics. The net effect of these changes is a poleward shift in the Southern Hemisphere jet by more than  $3^\circ$  and stronger stationary waves.

The jet shift is generally consistent with Sampe et al. (2010), though they imposed a zonally symmetric SST gradient of similar strength to that near the Agulhas Return Current in a zonally symmetric aquaplanet model. While it is tempting to conclude that most CMIP5 models lack the resolution to resolve the key processes in the Agulhas (and consistent with this, the jet latitude is typically too far equatorward), there is no statistically significant relationship between jet latitude and the strength of the surface temperature gradient in the region of Agulhas Return Current in CMIP5 models. This could be because the CMIP models show a strong connection between jet latitude and clouds (Ceppi et al. 2012, 2014) that potentially confounds any connection between the surface temperature gradient and jet latitude; in contrast, in the model we use here and in Sampe et al. (2010), cloud parameters are fixed among the experiments. Furthermore, roughly half of the CMIP5 models already simulate a surface temperature gradient in the

region of Agulhas Return Current as strong as that observed (Figs. 4 and 6), and so this factor cannot explain the bias for these models.

There is, however, a statistically significant relationship between the strength of the surface temperature gradient in the region of Agulhas Return Current and the strength of SH stationary waves in CMIP5. Specifically models with a stronger surface temperature gradient simulate stronger SH stationary waves both in CMIP5 and in our idealized model. This strengthening of stationary waves cannot be explained by analyzing changes in the Rossby wave source, by an increase in eddy activity, or by the change in jet latitude. Rather, it appears to be associated with the localization of the perturbation to the Indian Ocean basin.

SH stationary waves are of crucial importance for the stratospheric vortex (Wirth 1991; Scott and Haynes 2002). Comprehensive models have long suffered from a cold pole problem in the stratosphere, which complicates ozone forecasts: a cold pole leads to more ozone loss. Our results suggest that longstanding biases in the representation of the troposphere (and associated biases in precipitation, particularly in the tropics) may play a key role in this bias. Indeed, the simplified model integrations with better SH stationary waves exhibit a weaker vortex and warmer polar cap temperatures.

We have shown that common model biases in the representation of the Southern Hemisphere in general circulation models are linked: an ITCZ in the South Pacific leads to a degradation of stationary waves in the Southern Hemisphere, while an overly diffuse Agulhas is associated with too-weak stationary waves and an equatorward shift of the jet. Hence, progress toward removing the double-ITCZ bias and a better representation of the Agulhas Current should be expected to lead to an improved model representation of the extratropical large-scale circulation.

*Acknowledgments.* CIG, IW, and ME acknowledge the support of a European Research Council starting grant under the European Union Horizon 2020 Research and Innovation Programme (Grant Agreement 677756). EPG acknowledges support from the U.S. NSF through Grant AGS-1852727. MJ acknowledges support from the Australian Research Council (ARC) Centre of Excellence for Climate Extremes (CE170100023) and ARC Grant FL 150100035. We thank Ori Adam and three reviewers for helpful comments on an earlier version of this manuscript. Code for this model configuration will be made available on GitHub as part of the MiMA v2.0 release.

## APPENDIX

### A MiMA of Relevance to the Southern Hemisphere

We now document the changes made to MiMA as compared to Garfinkel et al. (2020b). Code for this model configuration will be made available on GitHub as part of the MiMA v2.0 release.

#### a. Land–sea contrast

As in Garfinkel et al. (2020b), we add three different aspects of land–sea contrast: the difference in mechanical damping

of near surface winds between the comparatively rough land surface versus the smooth ocean, the difference in evaporation between land and ocean, and the difference in heat capacity. The roughness lengths for momentum over ocean and land, and also for moisture exchange over ocean, is identical to that in Garfinkel et al. (2020b) and not repeated here for brevity. The roughness lengths for moisture exchange over land in Garfinkel et al. (2020b) was  $3.21 \times 10^{-17}$  m independent of latitude, which led to too much evaporation in the subtropics and not enough evaporation in the deep tropics when compared to reanalysis. Here, we have added latitudinal dependence to the representation of the roughness lengths for moisture over land, or  $z_{ohland}$  as follows:

$$z_{ohland} = 10^{-7} \exp\left(\frac{-|\phi|^3}{2 \times 15^\circ}\right) + 10^{-25} \exp\left(\frac{-|\phi - 45^\circ|^3}{2 \times 30^\circ}\right) + 10^{-25} \exp\left(\frac{-|\phi + 45^\circ|^3}{2 \times 30^\circ}\right) \text{ m}, \quad (\text{A1})$$

where  $\phi$  is latitude, which leads to increased evaporation near the equator. These parameters were selected via trial and error in order to generate reasonable evaporation for the most realistic experiment as compared to reanalysis data.

The heat capacity for land grid points is set to  $1 \times 10^7 \text{ J K}^{-1} \text{ m}^{-2}$  (equivalent to a mixed layer depth of 2.5 m). For oceanic grid points the heat capacity is set to

$$C_{\text{ocean}} = \begin{cases} 1 \times 10^8 \text{ J K}^{-1} \text{ m}^{-2}, & |\phi| < 20^\circ \\ 1 \times 10^8 \text{ J K}^{-1} \text{ m}^{-2} \times \left(1 - \frac{|\phi| - 20^\circ}{60^\circ - 20^\circ}\right) + 3 \times 10^8 \text{ J K}^{-1} \text{ m}^{-2} \times \left(\frac{|\phi| - 20^\circ}{60^\circ - 20^\circ}\right), & \text{otherwise,} \\ 3 \times 10^8 \text{ J K}^{-1} \text{ m}^{-2}, & |\phi| > 60^\circ \end{cases} \quad (\text{A2})$$

which corresponds to a mixed layer depth that smoothly increases from 25 m in the tropics to 75 m in polar regions. This reduction in the tropical mixed layer depth leads to a more realistic surface temperature and precipitation seasonal cycle as compared to the higher values used in Garfinkel et al. (2020b), as documented in Jucker (2019). Note that this option was included in the original MiMA release (Jucker 2017). For experiments with no land–sea contrast the oceanic mixed layer depth and roughness is used everywhere. We use a high-resolution land mask to determine land versus ocean; thus, the surface is accurately represented on the latitude versus longitude grid on which surface fluxes are computed.

For experiments with land–sea contrast, we set the albedo as

$$\text{albedo} = 0.23 + \frac{0.80 - 0.23}{2} \left[1 + \tanh\left(\frac{\phi - 68^\circ}{5^\circ}\right)\right] + \frac{0.80 - 0.23}{2} \left[1 - \tanh\left(\frac{\phi + 65^\circ}{5^\circ}\right)\right], \quad (\text{A3})$$

which leads to higher albedo values over the Arctic and Antarctic that smoothly transition to 0.23 in the midlatitudes and tropics, except for the following regions:

- 1) Australian desert:  $118^\circ < \lambda < 145^\circ$  and  $-30^\circ < \phi < -19^\circ$ ;
- 2) Gobi Desert:  $80^\circ < \lambda < 105^\circ$  and  $32^\circ < \phi < 40^\circ$ ;  $80^\circ < \lambda < 115^\circ$  and  $40^\circ \leq \phi < 52^\circ$ ; and
- 3) Saharan/Arabian Desert:  $345^\circ < \lambda$  or  $\lambda < 50^\circ$ ,  $13^\circ < \phi < 30^\circ$ ,

where the albedo is set to 0.43, and  $\lambda$  is longitude. The increased albedo over desert regions helps to ensure that the monsoon does not extend too far poleward into a region that is actually desert. A full discussion of the monsoons in MiMA is deferred to future work. MiMA has no clouds, and an albedo of 0.23 was primarily tuned to approximate the shortwave effects of clouds and lead to tropical surface temperature similar to those observed. For experiments with no land–sea contrast the

albedo is set to 0.27 everywhere in order to maintain a similar tropical surface temperature.

#### b. East–west ocean heat fluxes

Garfinkel et al. (2020b) introduced ocean horizontal heat uptake (often referred to as  $Q$  fluxes; e.g., Merlis et al. 2013) that mimicked those observed on the large scale. Here we specify  $Q$  fluxes on a much more regional scale in order to capture sharp surface temperature gradients associated with, for example, the Agulhas Current. These  $Q$  fluxes are necessary as we do not have a dynamical ocean. The net effect of these formulae is shown in Fig. 7, which compares favorably to the  $Q$  fluxes inferred from an ocean reanalysis by Forget and Ferreira (2019) (see their Fig. 1) or from a top-down Earth system energy budget in Trenberth et al. (2019) (see their Fig. 2) or Trenberth and Fasullo (2018) (see their Fig. 7). The only region in which we systematically deviate from the ocean heat uptake of Forget and Ferreira (2019) is the tropical Pacific, where we have heat diverging away and converging in the high latitudes Southern Hemisphere. The experiments in the text with and without a double ITCZ can be thought of as sensitivity tests to including such an ocean heat flux.

We now present the analytical formulae used to specify ocean heat fluxes. All integrations include the zonally uniform ocean horizontal heat uptake of Merlis et al. (2013), Jucker and Gerber (2017), and Garfinkel et al. (2020b), which is specified as

$$\nabla \cdot \mathbf{F}_o(\phi) = Q_o \frac{1}{\cos\phi} \left(1 - \frac{2\phi^2}{\phi_o^2}\right) \exp\left(-\frac{\phi^2}{\phi_o^2}\right), \quad (\text{A4})$$

with  $Q_o = 26 \text{ W m}^{-2}$  and  $\phi_o = 16^\circ$  [repeated from Eq. (A2) of Jucker and Gerber 2017; Merlis et al. 2013].

In addition, we prescribe several different components of the east–west ocean horizontal heat uptake. As described below, each individual component adds negligible net heating to the

TABLE A1. Parameters for the Agulhas following Eq. (A5).

| $A_n$ ( $\text{W m}^{-2}$ )                  | $\mu_{\lambda n}$ ( $^{\circ}$ longitude) | $\sigma_{\lambda n}$ ( $^{\circ}$ longitude) | $\mu_{\phi n}$ ( $^{\circ}$ latitude) | $\sigma_{\phi n}$ ( $^{\circ}$ latitude) |
|--|---|--|---------------------------------------|--|
| -30  | 28  | 10   | 18                                    | $\sqrt{50}$                              |
| -30  | 28  | 10   | -18                                   | $\sqrt{60}$                              |
| $-(38.5 + \text{Africaextra} \times 0.7709)$ | 11  | 2  | -15                                   | 10                                       |
| $+(83 + \text{Africaextra})$                 | 50  | 25   | -40                                   | 4  |
| $-(64.22 + \text{Africaextra} \times 1.3)$   | 50  | 20   | -48                                   | 4  |
| +20  | 14  | $\sqrt{30}$                                  | 0                                     | $\sqrt{50}$                              |
| +11  | 36  | $\sqrt{30}$                                  | 0                                     | $\sqrt{50}$                              |

atmosphere. When all are summed together, no net heating is added to the atmosphere (the residual heatings add up to zero). Specifically, anomalies in globally averaged surface temperature over the duration of the 38-yr CONTROL integration are less than 0.3 K (i.e., the model is fully spun up and does not drift). Many of the perturbations described below are of the form

$$\nabla \cdot \mathbf{F} = \sum A_n \exp\left[-\frac{(\lambda - \mu_{\lambda n})^2}{2\sigma_{\lambda n}^2}\right] \exp\left[-\frac{(\phi - \mu_{\phi n})^2}{2\sigma_{\phi n}^2}\right], \quad (\text{A5})$$

$$\nabla \cdot \mathbf{F}_{\text{Africa}} = \begin{cases} 25 \text{ W m}^{-2} \times \left[1 - \left(\frac{\phi}{35^{\circ}}\right)^2\right] \cos[5(\lambda - 28^{\circ})], & 10^{\circ} \leq \lambda \leq 82^{\circ} \text{ and } |\phi| < 35^{\circ} \\ 0, & \text{otherwise} \end{cases} \quad (\text{A6})$$

Finally, we add heat to the atmosphere near the African coast, by specifying

$$\nabla \cdot \mathbf{F}_{\text{Agulhas}} = \begin{cases} +[(38 + \text{Africaextra})/3] \text{ W m}^{-2} \\ \times \exp\left[-\frac{(\lambda - \frac{2}{3}\phi - 57^{\circ})^2}{2 \times 4^{\circ 2}}\right] \exp\left[-\frac{(\lambda + \phi - 10^{\circ})^2}{2 \times 15^{\circ 2}}\right], \end{cases} \quad (\text{A7})$$

in the region  $2^{\circ} \leq \lambda \leq 100^{\circ}$  and  $-60^{\circ} \leq \phi \leq 35^{\circ}$ .

Africaextra is alternately set to 70 or  $-70 \text{ W m}^{-2}$  in section 5. For the simulations with a zonally symmetric

$$\nabla \cdot \mathbf{F}_{\text{Pac}} = \begin{cases} \left[1 - \left(\frac{\phi}{35^{\circ}}\right)^4\right] Q_{\text{Pacific}} \cos[5/3(\lambda - 140^{\circ})], & 86^{\circ} \leq \lambda \leq 302^{\circ} \text{ and } |\phi| < 35^{\circ} \\ 0, & \text{otherwise} \end{cases}, \quad (\text{A9})$$

as a first step onto which we add smaller-scale features in order to represent observed ocean heat fluxes, with  $Q_{\text{Pacific}} = 18 \text{ W m}^{-2}$ .

and for these perturbations we include tables of the parameters  $A_n$ ,  $\mu_{\lambda n}$ ,  $\sigma_{\lambda n}$ ,  $\mu_{\phi n}$ , and  $\sigma_{\phi n}$ .

### c. Agulhas Current

The representation of the Agulhas Current, Agulhas Leakage, the Agulhas Return Current, cold upwelling off the coast of Namibia, and a cooler tropical west Indian Ocean in the region  $2^{\circ} \leq \lambda \leq 100^{\circ}$  and  $-60^{\circ} \leq \phi \leq 35^{\circ}$  is specified with the parameters in Table A1 applied to Eq. (A5).

To ensure that there is little cooling over tropical Africa and weak cooling over the tropical west Indian Ocean, we additionally specify

Agulhas perturbation, Sampeterm is alternately set to 25 or  $-25 \text{ W m}^{-2}$  and the perturbation is specified as

$$\nabla \cdot \mathbf{F}_{\text{Agulhas}} = \begin{cases} +\text{Sampeterm} \times 0.8822 \text{ W m}^{-2} \times \exp\left[-\frac{(\phi + 40^{\circ})^2}{2 \times 4^{\circ 2}}\right], \\ -\text{Sampeterm} \times \exp\left[-\frac{(\phi + 48^{\circ})^2}{2 \times 4^{\circ 2}}\right], \\ 0, & \text{otherwise} \end{cases} \quad (\text{A8})$$

### d. Pacific sector

We begin with a representation of the Pacific warm pool similar to that in Garfinkel et al. (2020b):

To better confine the cold tongue to oceanic regions, we include

TABLE A2. Parameters for the cold tongue following Eq. (A5).

| $A_n$ ( $\text{W m}^{-2}$ )   | $\mu_{\lambda n}$ ( $^{\circ}$ longitude) | $\sigma_{\lambda n}$ ( $^{\circ}$ longitude) | $\mu_{\phi n}$ ( $^{\circ}$ latitude) | $\sigma_{\phi n}$ ( $^{\circ}$ latitude) |
|-------------------------------|---|--|---------------------------------------|--|
| -(50 - ITCZEW $\times$ 0.28)  | 270                                       | 9  | 0                                     | 3  |
| -(50 - ITCZEW $\times$ 0.28)  | 250                                       | 9  | -1                                    | 3  |
| -(50 - ITCZEW $\times$ 0.28)  | 230                                       | 9  | -2                                    | 3  |
| -39                           | 210                                       | 9  | -2                                    | 3  |
| -36                           | 190                                       | 9  | 0                                     | 3  |
| -16                           | 170                                       | 9  | 0                                     | 3  |
| -40                           | 287                                       | 2  | -25                                   | 9  |
| -15                           | 282                                       | 5  | -15                                   | 9  |
| -(25 + ITCZNS + ITCZEW)       | 240                                       | 40   | -21                                   | 11                                       |
| -38                           | 195                                       | 13   | 16                                    | 7  |
| -51.4                         | 225                                       | 13   | 16                                    | 7  |
| +28.2                         | 220                                       | 40   | -57                                   | 15                                       |
| +(14 + ITCZEW $\times$ 0.9)   | 165                                       | 20   | -20                                   | 5  |
| +(16 + ITCZEW $\times$ 0.9)   | 195                                       | 20   | -33                                   | 7  |
| +(50 + ITCZEW $\times$ 0.9)   | 155                                       | 3  | -30                                   | 7  |
| +(40 + ITCZEW $\times$ 0.9)   | 180                                       | 5  | -40                                   | 5  |
| +41                           | 240                                       | 30   | -62                                   | 8  |
| +60                           | 180                                       | 13   | 6.97                                  | 2  |
| +47                           | 210                                       | 13   | 6.97                                  | 2  |
| +45                           | 240                                       | 13   | 6.97                                  | 2  |
| +(19.5 + ITCZEW $\times$ 0.3) | 145                                       | 14   | 3                                     | 4  |
| +(40 + ITCZEW $\times$ .25)   | 150                                       | 13   | 7                                     | 3  |

$$\nabla \cdot \mathbf{F}_{\text{CTpart1}} = \begin{cases} \left[ 1 - \left( \frac{\phi}{35^{\circ}} \right)^4 \right] Q_{\text{Pacific}} \sin[8(\lambda - 279.5^{\circ})], & 257^{\circ} \leq \lambda \leq 302^{\circ} \text{ and } |\phi| < 35^{\circ} \\ 0, & \text{otherwise} \end{cases} \quad (\text{A10})$$

The representation of the cold tongue is made more realistic by fluxing heat out of the equatorial east Pacific and toward the west Pacific and subpolar South Pacific. In the region  $129^{\circ} \leq \lambda \leq 290^{\circ}$  and  $-78^{\circ} \geq \phi \geq 24^{\circ}$ , we specify the parameters in Table A2 applied to Eq. (A5).

ITCZNS and ITCZEW are the parameters modified in section 4. ITCZEW is alternately set to 30 or  $-30 \text{ W m}^{-2}$ , and ITCZNS is alternately set to 25 or  $-25 \text{ W m}^{-2}$ .

The subpolar perturbation for ITCZNS is specified in the region  $-65^{\circ} \leq \phi \leq 45^{\circ}$  as

$$\nabla \cdot \mathbf{F}_{\text{ITCZNS}} = +\text{ITCZNS} \times 0.74537 \text{ W m}^{-2} \times \exp \left[ -\frac{(\phi + 55^{\circ})^2}{2 \times 7^{\circ 2}} \right]. \quad (\text{A11})$$

The west Pacific perturbation for ITCZEW also includes the additional term in the region  $50^{\circ} \leq \lambda \leq 220^{\circ}$  and  $-36^{\circ} \leq \phi \leq 10^{\circ}$ :

$$\nabla \cdot \mathbf{F}_{\text{ITCZEW}} = +\text{ITCZEW} \times 0.61054 \text{ W m}^{-2} \times \exp \left[ -\frac{(\lambda - 115^{\circ})^2}{2 \times 16^{\circ 2}} \right] \exp \left[ -\frac{(\phi + 3^{\circ})^2}{2 \times 11^{\circ 2}} \right]. \quad (\text{A12})$$

To avoid strong oceanic heat uptake over regions that are actually continents, we modify the heat flux near Australia. Over the region  $50^{\circ} \leq \lambda \leq 220^{\circ}$  and  $-36^{\circ} \leq \phi \leq 10^{\circ}$ , we specify the parameters in Table A3 applied to Eq. (A5). The net effect of this is to prevent a flux of heat into the atmosphere over subtropical Australia that would otherwise be imposed in Eq. (A9). This extra heat flux into the atmosphere instead occurs over the Indian Ocean, and thus represents Indonesian Throughflow.

To represent the Kuroshio, we add in the region  $110^{\circ} \leq \lambda \leq 270^{\circ}$  and  $5^{\circ} \geq \phi \leq 47^{\circ}$ :

$$\nabla \cdot \mathbf{F}_{\text{Kuroshio}} = \begin{cases} Q_{\text{Kuroshio}} \exp \left[ -\frac{(\lambda - 3\phi - 45^{\circ})^2}{2 \times 10^{\circ 2}} \right] \exp \left[ -\frac{(\lambda + \phi - 170^{\circ})^2}{2 \times 20^{\circ 2}} \right], \\ -Q_{\text{Kuroshio}} 0.594 \times \exp \left[ -\frac{(\lambda + \phi - 268^{\circ})^2}{2 \times 7^{\circ 2}} \right] \exp \left[ -\frac{(\lambda - \phi - 215^{\circ})^2}{2 \times 25^{\circ 2}} \right], \\ 0, & \text{otherwise} \end{cases} \quad (\text{A13})$$

TABLE A3. Parameters for Australia following Eq. (A5).

| $A_n$ ( $\text{W m}^{-2}$ )       | $\mu_{\lambda n}$ ( $^\circ$ longitude) | $\sigma_{\lambda n}$ ( $^\circ$ longitude) | $\mu_{\phi n}$ ( $^\circ$ latitude) | $\sigma_{\phi n}$ ( $^\circ$ latitude) |
|-----------------------------------|---|--|-------------------------------------|--|
| $-1.02(Q_{\text{Pacific}} + Q_o)$ | 135                                     | 15   | -20                                 | 6                                      |
| -10                               | 147                                     | 8  | -27                                 | 7                                      |
| +16.6                             | 120                                     | 30   | -20                                 | 6                                      |
| +27.89                            | 100                                     | 10   | -10                                 | 4                                      |
| +4.9                              | 135                                     | 15   | 0                                   | 4                                      |

where  $Q_{\text{Kuroshio}} = 40 \text{ W m}^{-2}$ . Equation (A13) describes a flux of heat out of the far eastern Pacific near the coast of Mexico and the United States toward the far west Pacific, and the two components nearly cancel and so add minimal net heat to the atmosphere.

The representation of the Kuroshio is made more regional by fluxing heat away from regions of the subtropics where the observed Kuroshio does not reach. For the region  $70^\circ \leq \lambda \leq 240^\circ$  and  $-10^\circ \geq \phi \geq 60^\circ$ , we specify the parameters in Table A4 applied to Eq. (A5), plus the additional perturbation in Eq. (A14):

$$\nabla \cdot \mathbf{F}_{\text{Kuroshio2}} = \left\{ +49.5 \left[ \frac{(\lambda - 3\phi - 45^\circ)^2}{2 \times 10^{02}} \right] \exp \left[ -\frac{(\lambda + \phi - 160^\circ)^2}{2 \times 20^{02}} \right], \right. \quad (\text{A14})$$

#### e. Atlantic sector

The representation of the Gulf Current is

$$\nabla \cdot \mathbf{F}_{\text{Gulf}} = \begin{cases} 70 \text{ W m}^{-2} \times \exp \left[ -\frac{(\lambda - 2\phi - 220^\circ)^2}{2 \times 3^{02}} \right] \exp \left[ -\frac{(\lambda + \phi - 335^\circ)^2}{2 \times 25^{02}} \right], & 275^\circ \leq \lambda \leq 335^\circ \text{ and } 10^\circ \leq \phi \leq 52^\circ \\ -63.9 \text{ W m}^{-2} \times \exp \left[ -\frac{(\lambda - 0.5\phi - 325^\circ)^2}{2 \times 3^{02}} \right] \exp \left[ -\frac{(\phi - 25^\circ)^2}{2 \times 7^{02}} \right], & 298^\circ \leq \lambda \leq 358^\circ \text{ and } 10^\circ \leq \phi \leq 52^\circ \\ 0, & \text{otherwise} \end{cases} \quad (\text{A15})$$

Equation (A15) describes a flux of heat out of the far eastern Atlantic toward the far west Atlantic, and the two components nearly cancel and so add minimal net heat to the atmosphere.

Heat is also fluxed out of the tropical Atlantic and toward the Gulf Stream and Norwegian Sea:

$$\nabla \cdot \mathbf{F}_{\text{Atl}} = \begin{cases} -50 \text{ W m}^{-2} \left\{ \exp \left[ -\frac{(\lambda - 342^\circ)^2}{2 \times 9^{02}} \right] + \exp \left[ -\frac{(\lambda - 0^\circ)^2}{2 \times 8^{02}} \right] \right\} \exp \left[ -\frac{(\phi + 5^\circ)^2}{2 \times 5^{02}} \right], & 275^\circ \leq \lambda \leq 18^\circ, \quad -35^\circ \leq \phi \leq 77^\circ \\ -12.6 \text{ W m}^{-2} \times \exp \left[ -\frac{(\lambda - 345^\circ)^2}{2 \times 16^{02}} \right] \exp \left[ -\frac{(\phi + 16^\circ)^2}{2 \times 8^{02}} \right], & 275^\circ \leq \lambda, \quad -35^\circ \leq \phi \leq 77^\circ \\ +54.732 \text{ W m}^{-2} \times \exp \left[ -\frac{(\lambda - 2\phi - 220^\circ)^2}{2 \times 10^{02}} \right] \exp \left[ -\frac{(\lambda + \phi - 375^\circ)^2}{2 \times 30^{02}} \right], & 275^\circ \leq \lambda, \quad -35^\circ \leq \phi \leq 77^\circ \\ +64.2857 \text{ W m}^{-2} \times \cos[3(\lambda - 348^\circ)] \left[ 1 - \left( \frac{\phi - 67^\circ}{10^\circ} \right)^4 \right], & 318^\circ \leq \lambda \leq 18^\circ, \quad 57^\circ \leq \phi \leq 77^\circ \\ 0, & \text{otherwise} \end{cases} \quad (\text{A16})$$

TABLE A4. Parameters for the Kuroshio following Eq. (A5).

| $A_n$ ( $\text{W m}^{-2}$ ) | $\mu_{\lambda n}$ ( $^\circ$ longitude) | $\sigma_{\lambda n}$ ( $^\circ$ longitude) | $\mu_{\phi n}$ ( $^\circ$ latitude) | $\sigma_{\phi n}$ ( $^\circ$ latitude) |
|-----------------------------|---|--|-------------------------------------|--|
| -27.60                      | 140                                     | 39   | 19.7                                | 7                                      |
| -5.2                        | 140                                     | 8  | 20                                  | 4                                      |
| +35.4                       | 160                                     | 20   | 35                                  | 6                                      |
| +22.9                       | 90                                      | 12   | 0                                   | 5                                      |

TABLE A5. Parameters for South America following Eq. (A5).

| $A_n$ ( $\text{W m}^{-2}$ ) | $\mu_{\lambda n}$ ( $^\circ$ longitude) | $\sigma_{\lambda n}$ ( $^\circ$ longitude) | $\mu_{\phi n}$ ( $^\circ$ latitude) | $\sigma_{\phi n}$ ( $^\circ$ latitude) |
|-----------------------------|---|--|-------------------------------------|--|
| $-0.92Q_o$                  | 290                                     | 20   | -20                                 | 7                                      |
| -16.8                       | 325                                     | 22   | 19.5                                | 8                                      |
| $+1.2Q_o$                   | 270                                     | 7  | 22                                  | 5                                      |
| $+1.58Q_o$                  | 283                                     | 5  | 0                                   | 6                                      |
| $+1.06415Q_o$               | 304                                     | 6  | -2                                  | 7                                      |
| $+0.85Q_o$                  | 284                                     | 5  | -10                                 | 6                                      |
| $+0.63Q_o$                  | 317                                     | 5  | -6                                  | 4                                      |
| +42.54                      | 325                                     | 11   | +4.2                                | 2                                      |

To avoid strong oceanic heat flux over regions that are actually continents, we modify the heat flux over South America as follows. Over the region  $250^\circ \leq \lambda \leq 344^\circ$  and  $-35^\circ \leq \phi \leq 40^\circ$ , we specify the parameters in Table A5 applied to Eq. (A5). The net effect of this is to flux heat out of subtropical South America and also out of the subtropical North Atlantic and to converge heat into the Caribbean Sea and toward equatorial South America that otherwise has heat fluxed away due to Eqs.

(A9) and (A16). The components nearly cancel and so add minimal net heat to the atmosphere.

To represent the Brazil and Falkland Current, a dipole is added in the South Atlantic. Over the region  $290^\circ \leq \lambda$  and  $-61^\circ \leq \phi \leq -30^\circ$ , we specify the parameters in Table A6 applied to Eq. (A5).

Additional heat is fluxed toward the Norwegian and Barents Sea and away from land grid points in subtropical Africa as follows:

$$\nabla \cdot \mathbf{F}_{\text{Barents1}} = \begin{cases} 68.0 \text{ W m}^{-2} \left[ 1 - \left( \frac{\phi - 76^\circ}{6.5^\circ} \right)^4 \right] \cos[2(\lambda - 30^\circ)], & 345^\circ \leq \lambda \leq 75^\circ \text{ and } 71^\circ \leq \phi \leq 83^\circ \\ -14.5 \text{ W m}^{-2} \times \exp \left[ -\frac{(\lambda - 357^\circ)^2}{2 \times 20^{o2}} \right] \exp \left[ -\frac{(\phi - 20^\circ)^2}{2 \times 7^{o2}} \right], & 310^\circ \leq \lambda \leq 30^\circ \text{ and } 10^\circ \leq \phi \leq 35^\circ \\ 0, & \text{otherwise} \end{cases} \quad (\text{A17})$$

The components nearly cancel and so add minimal net heat to the atmosphere.

The representation of heat flux into the Norwegian and Barents Sea is further increased as follows:

$$\nabla \cdot \mathbf{F}_{\text{Barents2}} = \begin{cases} 25.0 \text{ W m}^{-2} \left[ 1 - \left( \frac{\phi - 76^\circ}{7^\circ} \right)^4 \right] \cos(\lambda - 10^\circ), & 69^\circ \leq \phi \leq 83^\circ \\ 68.2 \text{ W m}^{-2} \left[ 1 - \left( \frac{\phi - 68^\circ}{8^\circ} \right)^4 \right] \cos[6(\lambda - 2^\circ)], & 347^\circ \leq \lambda \leq 17^\circ, 60^\circ \leq \phi \leq 76^\circ \\ -38 \text{ W m}^{-2} \exp \left[ -\frac{(\lambda - 2\phi - 152^\circ)^2}{2 \times 10^{o2}} \right] \exp \left[ -\frac{(\lambda + \phi - 342^\circ)^2}{2 \times 20^{o2}} \right], & 260^\circ \leq \lambda \leq 310^\circ, 55^\circ \leq \phi \leq 85^\circ \\ -100 \text{ W m}^{-2} \times \exp \left[ -\frac{(\lambda - 275^\circ)^2}{2 \times 5^{o2}} \right] \exp \left[ -\frac{(\phi - 58^\circ)^2}{2 \times 4^{o2}} \right], & 260^\circ \leq \lambda \leq 310^\circ, 55^\circ \leq \phi \leq 85^\circ \\ 10.8 \text{ W m}^{-2} \times \exp \left[ -\frac{(\lambda - 2\phi - 220^\circ)^2}{2 \times 10^{o2}} \right] \exp \left[ -\frac{(\lambda + \phi - 335^\circ)^2}{2 \times 25^{o2}} \right], & 275^\circ \leq \lambda \leq 335^\circ, 10^\circ \geq \phi \leq 52^\circ \\ 0, & \text{otherwise} \end{cases} \quad (\text{A18})$$

TABLE A6. Parameters for the South Atlantic following Eq. (A5).

| $A_n$ ( $\text{W m}^{-2}$ ) | $\mu_{\lambda n}$ ( $^\circ$ longitude) | $\sigma_{\lambda n}$ ( $^\circ$ longitude) | $\mu_{\phi n}$ ( $^\circ$ latitude) | $\sigma_{\phi n}$ ( $^\circ$ latitude) |
|-----------------------------|---|--|-------------------------------------|--|
| +37.4                       | 323                                     | 11   | -36                                 | 4                                      |
| -40                         | 311                                     | 11   | -45                                 | 4                                      |

The components nearly cancel and so add minimal net heat to the atmosphere. This specification represents a divergence of heat away from the Chukchi and Beaufort Seas and Hudson Bay and Baffin Bay, and convergence in the Norwegian and Barents Sea, in order to better capture the pattern of surface temperature. Note that we specify a zonally symmetric albedo, while in reality, sea ice coverage is less extensive in the Norwegian and Barents Seas as compared to similar latitudes elsewhere.

## REFERENCES

- AchutaRao, K., and K. R. Sperber, 2006: ENSO simulation in coupled ocean-atmosphere models: Are the current models better? *Climate Dyn.*, **27**, 1–15, <https://doi.org/10.1007/s00382-006-0119-7>.
- Adam, O., T. Schneider, F. Briant, and T. Bischoff, 2016: Relation of the double-ITCZ bias to the atmospheric energy budget in climate models. *Geophys. Res. Lett.*, **43**, 7670–7677, <https://doi.org/10.1002/2016GL069465>.
- , —, and —, 2018: Regional and seasonal variations of the double-ITCZ bias in CMIP5 models. *Climate Dyn.*, **51**, 101–117, <https://doi.org/10.1007/s00382-017-3909-1>.
- Adler, R. F., and Coauthors, 2003: The Version-2 Global Precipitation Climatology Project (GPCP) monthly precipitation analysis (1979–present). *J. Hydrometeorol.*, **4**, 1147–1167, [https://doi.org/10.1175/1525-7541\(2003\)004<1147:TVGPCP>2.0.CO;2](https://doi.org/10.1175/1525-7541(2003)004<1147:TVGPCP>2.0.CO;2).
- Alexander, M., and T. Dunkerton, 1999: A spectral parameterization of mean-flow forcing due to breaking gravity waves. *J. Atmos. Sci.*, **56**, 4167–4182, [https://doi.org/10.1175/1520-0469\(1999\)056<4167:ASPOMF>2.0.CO;2](https://doi.org/10.1175/1520-0469(1999)056<4167:ASPOMF>2.0.CO;2).
- , and A. Grimsdell, 2013: Seasonal cycle of orographic gravity wave occurrence above small islands in the Southern Hemisphere: Implications for effects on the general circulation. *J. Geophys. Res. Atmos.*, **118**, 11 589–11 599, <https://doi.org/10.1002/2013JD020526>.
- Bayr, T., D. I. Domeisen, and C. Wengel, 2019: The effect of the equatorial Pacific cold SST bias on simulated ENSO teleconnections to the North Pacific and California. *Climate Dyn.*, **53**, 3771–3789, <https://doi.org/10.1007/S00382-019-04746-9>.
- Bellenger, H., É. Guilyardi, J. Leloup, M. Lengaigne, and J. Vialard, 2014: ENSO representation in climate models: From CMIP3 to CMIP5. *Climate Dyn.*, **42**, 1999–2018, <https://doi.org/10.1007/s00382-013-1783-z>.
- Betts, A. K., 1986: A new convective adjustment scheme. Part I: Observational and theoretical basis. *Quart. J. Roy. Meteor. Soc.*, **112**, 677–691, <https://doi.org/10.1002/QJ.49711247307>.
- , and M. J. Miller, 1986: A new convective adjustment scheme. Part II: Single column tests using GATE wave, BOMEX, ATEX and Arctic air-mass data sets. *Quart. J. Roy. Meteor. Soc.*, **112**, 693–709, <https://doi.org/10.1002/QJ.49711247308>.
- Bracegirdle, T. J., E. Shuckburgh, J.-B. Sallee, Z. Wang, A. J. Meijers, N. Bruneau, T. Phillips, and L. J. Wilcox, 2013: Assessment of surface winds over the Atlantic, Indian, and Pacific Ocean sectors of the Southern Ocean in CMIP5 models: Historical bias, forcing response, and state dependence. *J. Geophys. Res. Atmos.*, **118**, 547–562, <https://doi.org/10.1002/JGRD.50153>.
- Ceppi, P., Y.-T. Hwang, D. M. Frierson, and D. L. Hartmann, 2012: Southern Hemisphere jet latitude biases in CMIP5 models linked to shortwave cloud forcing. *Geophys. Res. Lett.*, **39**, L19708, <https://doi.org/10.1029/2012GL053115>.
- , M. D. Zelinka, and D. L. Hartmann, 2014: The response of the Southern Hemispheric eddy-driven jet to future changes in shortwave radiation in CMIP5. *Geophys. Res. Lett.*, **41**, 3244–3250, <https://doi.org/10.1002/2014GL060043>.
- Cohen, N. Y., E. P. Gerber, and E. P. Oliver Bühler, 2013: Compensation between resolved and unresolved wave driving in the stratosphere: Implications for downward control. *J. Atmos. Sci.*, **70**, 3780–3798, <https://doi.org/10.1175/JAS-D-12-0346.1>.
- Curtis, P. E., P. Ceppi, and G. Zappa, 2020: Role of the mean state for the Southern Hemispheric jet stream response to CO<sub>2</sub> forcing in CMIP6 models. *Environ. Res. Lett.*, **15**, 064011, <https://doi.org/10.1088/1748-9326/ab8331>.
- Eyring, V., T. Shepherd, and D. Waugh, Eds., 2010: SPARC CCMVal report on the evaluation of chemistry-climate models. SPARC Rep. 5, WCRP-30/2010, WMO/TD No. 40, 426 pp., <https://www.sparc-climate.org/publications/sparc-reports/sparc-report-no-5/>.
- Forget, G., and D. Ferreira, 2019: Global ocean heat transport dominated by heat export from the tropical Pacific. *Nat. Geosci.*, **12**, 351–354, <https://doi.org/10.1038/s41561-019-0333-7>.
- Frierson, D. M., I. M. Held, and P. Zurita-Gotor, 2006: A gray-radiation aquaplanet moist GCM. Part I: Static stability and eddy scale. *J. Atmos. Sci.*, **63**, 2548–2566, <https://doi.org/10.1175/JAS3753.1>.
- , —, and —, 2007: A gray-radiation aquaplanet moist GCM. Part II: Energy transports in altered climates. *J. Atmos. Sci.*, **64**, 1680–1693, <https://doi.org/10.1175/JAS3913.1>.
- Garfinkel, C. I., and L. D. Oman, 2018: Effect of gravity waves from small islands in the Southern Ocean on the Southern Hemisphere atmospheric circulation. *J. Geophys. Res. Atmos.*, **123**, 1552–1561, <https://doi.org/10.1002/2017JD027576>.
- , —, E. A. Barnes, D. W. Waugh, M. M. Hurwitz, and A. M. Molod, 2013a: Connections between the spring breakup of the Southern Hemisphere polar vortex, stationary waves, and air-sea roughness. *J. Atmos. Sci.*, **70**, 2137–2151, <https://doi.org/10.1175/JAS-D-12-0242.1>.
- , D. W. Waugh, and E. P. Gerber, 2013b: The effect of tropospheric jet latitude on coupling between the stratospheric polar vortex and the troposphere. *J. Climate*, **26**, 2077–2095, <https://doi.org/10.1175/JCLI-D-12-00301.1>.
- , O. Adam, E. Morin, Y. Enzel, E. Elbaum, M. Bartov, D. Rostkier-Edelstein, and U. Dayan, 2020a: The role of zonally averaged climate change in contributing to inter-model spread in CMIP5 predicted local precipitation changes. *J. Climate*, **33**, 1141–1154, <https://doi.org/10.1175/JCLI-D-19-0232.1>.
- , J. P. White, E. P. Gerber, and M. Jucker, 2020b: The building blocks of Northern Hemisphere wintertime stationary waves. *J. Climate*, **33**, 5611–5633, <https://doi.org/10.1175/JCLI-D-19-0181.1>.
- He, J., and B. J. Soden, 2016: The impact of SST biases on projections of anthropogenic climate change: A greater role for atmosphere-only models? *Geophys. Res. Lett.*, **43**, 7745–7750, <https://doi.org/10.1002/2016GL069803>.
- Held, I. M., and B. J. Soden, 2006: Robust responses of the hydrological cycle to global warming. *J. Climate*, **19**, 5686–5699, <https://doi.org/10.1175/JCLI3990.1>.
- Holton, L., J. Deshayes, B. Backeberg, B. Loveday, J. Hermes, and C. Reason, 2017: Spatio-temporal characteristics of Agulhas Leakage: A model inter-comparison study. *Climate Dyn.*, **48**, 2107–2121, <https://doi.org/10.1007/s00382-016-3193-5>.
- Honda, M., K. Yamazaki, H. Nakamura, and K. Takeuchi, 1999: Dynamic and thermodynamic characteristics of atmospheric response to anomalous sea-ice extent in the Sea of Okhotsk. *J. Climate*, **12**, 3347–3358, [https://doi.org/10.1175/1520-0442\(1999\)012<3347:DATCOA>2.0.CO;2](https://doi.org/10.1175/1520-0442(1999)012<3347:DATCOA>2.0.CO;2).
- Hubert, L., A. Krueger, and J. Winston, 1969: The double intertropical convergence zone—Fact or fiction? *J. Atmos. Sci.*, **26**, 771–

- 773, [https://doi.org/10.1175/1520-0469\(1969\)026<0771:TDICZF>2.0.CO;2](https://doi.org/10.1175/1520-0469(1969)026<0771:TDICZF>2.0.CO;2).
- Hurwitz, M. M., P. A. Newman, F. Li, L. D. Oman, O. Morgenstern, P. Braesicke, and J. A. Pyle, 2010: Assessment of the breakup of the Antarctic polar vortex in two new chemistry-climate models. *J. Geophys. Res.*, **115**, D07105, <https://doi.org/10.1029/2009JD012788>.
- Hwang, Y.-T., and D. M. Frierson, 2013: Link between the double-intertropical convergence zone problem and cloud biases over the Southern Ocean. *Proc. Natl. Acad. Sci. USA*, **110**, 4935–4940, <https://doi.org/10.1073/pnas.1213302110>.
- Iacono, M. J., E. J. Mlawer, S. A. Clough, and J.-J. Morcrette, 2000: Impact of an improved longwave radiation model, RRTM, on the energy budget and thermodynamic properties of the NCAR community climate model, CCM3. *J. Geophys. Res.*, **105**, 14 873–14 890, <https://doi.org/10.1029/2000JD900091>.
- Inatsu, M., and B. J. Hoskins, 2004: The zonal asymmetry of the Southern Hemisphere winter storm track. *J. Climate*, **17**, 4882–4892, <https://doi.org/10.1175/JCLI-3232.1>.
- James, I., 1988: On the forcing of planetary-scale Rossby waves by Antarctica. *Quart. J. Roy. Meteor. Soc.*, **114**, 619–637, <https://doi.org/10.1002/qj.49711448105>.
- Jucker, M., 2017: mjucker/mima: Mima v1.0. Accessed 9 September 2020, <https://doi.org/10.5281/zenodo.321708>.
- , 2019: The surface of an aquaplanet GCM. *Iceberg*, <https://doi.org/10.5281/zenodo.3358284>.
- , and E. Gerber, 2017: Untangling the annual cycle of the tropical tropopause layer with an idealized moist model. *J. Climate*, **30**, 7339–7358, <https://doi.org/10.1175/JCLI-D-17-0127.1>.
- Karpechko, A. Y., and Coauthors, 2018: Stratospheric ozone changes and climate. Scientific Assessment of Ozone Depletion, Global Ozone Research and Monitoring Project Rep. 58, 5.1–5.69.
- Kay, J. E., C. Wall, V. Yettella, B. Medeiros, C. Hannay, P. Caldwell, and C. Bitz, 2016: Global climate impacts of fixing the Southern Ocean shortwave radiation bias in the Community Earth System Model (CESM). *J. Climate*, **29**, 4617–4636, <https://doi.org/10.1175/JCLI-D-15-0358.1>.
- Kidston, J., and E. P. Gerber, 2010: Intermodel variability of the poleward shift of the austral jet stream in the CMIP3 integrations linked to biases in 20th century climatology. *Geophys. Res. Lett.*, **37**, L09708, <https://doi.org/10.1029/2010GL042873>.
- Knutti, R., and J. Sedláček, 2013: Robustness and uncertainties in the new CMIP5 climate model projections. *Nat. Climate Change*, **3**, 369–373, <https://doi.org/10.1038/nclimate1716>.
- Kwon, Y.-O., M. A. Alexander, N. A. Bond, C. Frankignoul, H. Nakamura, B. Qiu, and L. A. Thompson, 2010: Role of the Gulf Stream and Kuroshio–Oyashio systems in large-scale atmosphere–ocean interaction: A review. *J. Climate*, **23**, 3249–3281, <https://doi.org/10.1175/2010JCLI3343.1>.
- Li, G., and S.-P. Xie, 2014: Tropical biases in CMIP5 multimodel ensemble: The excessive equatorial Pacific cold tongue and double ITCZ problems. *J. Climate*, **27**, 1765–1780, <https://doi.org/10.1175/JCLI-D-13-00337.1>.
- , —, Y. Du, and Y. Luo, 2016: Effects of excessive equatorial cold tongue bias on the projections of tropical Pacific climate change. Part I: The warming pattern in CMIP5 multi-model ensemble. *Climate Dyn.*, **47**, 3817–3831, <https://doi.org/10.1007/s00382-016-3043-5>.
- Lin, J.-L., 2007: The double-ITCZ problem in IPCC AR4 coupled GCMs: Ocean–atmosphere feedback analysis. *J. Climate*, **20**, 4497–4525, <https://doi.org/10.1175/JCLI4272.1>.
- Lin, P., D. Paynter, L. Polvani, G. J. Correa, Y. Ming, and V. Ramaswamy, 2017: Dependence of model-simulated response to ozone depletion on stratospheric polar vortex climatology. *Geophys. Res. Lett.*, **44**, 6391–6398, <https://doi.org/10.1002/2017GL073862>.
- Lindberg, C., and A. J. Broccoli, 1996: Representation of topography in spectral climate models and its effect on simulated precipitation. *J. Climate*, **9**, 2641–2659, [https://doi.org/10.1175/1520-0442\(1996\)009<2641:ROTISC>2.0.CO;2](https://doi.org/10.1175/1520-0442(1996)009<2641:ROTISC>2.0.CO;2).
- Liu, W. T., X. Xie, and P. P. Niiler, 2007: Ocean–atmosphere interaction over Agulhas extension meanders. *J. Climate*, **20**, 5784–5797, <https://doi.org/10.1175/2007JCLI1732.1>.
- Luo, J.-J., S. Masson, E. Roeckner, G. Madec, and T. Yamagata, 2005: Reducing climatology bias in an ocean–atmosphere CGCM with improved coupling physics. *J. Climate*, **18**, 2344–2360, <https://doi.org/10.1175/JCLI3404.1>.
- Lutjeharms, J., 2007: Three decades of research on the greater Agulhas Current. *Ocean Sci.*, **3**, 129–147, <https://doi.org/10.5194/os-3-129-2007>.
- Matsueda, M., and T. N. Palmer, 2011: Accuracy of climate change predictions using high resolution simulations as surrogates of truth. *Geophys. Res. Lett.*, **38**, L05803, <https://doi.org/10.1029/2010GL046618>.
- Mbengue, C., and T. Schneider, 2017: Storm-track shifts under climate change: Toward a mechanistic understanding using baroclinic mean available potential energy. *J. Atmos. Sci.*, **74**, 93–110, <https://doi.org/10.1175/JAS-D-15-0267.1>.
- McLandress, C., T. G. Shepherd, S. Polavarapu, and S. R. Beagley, 2012: Is missing orographic gravity wave drag near 60°S the cause of the stratospheric zonal wind biases in chemistry-climate models? *J. Atmos. Sci.*, **69**, 802–818, <https://doi.org/10.1175/JAS-D-11-0159.1>.
- Mechoso, C. R., and Coauthors, 1995: The seasonal cycle over the tropical Pacific in coupled ocean–atmosphere general circulation models. *Mon. Wea. Rev.*, **123**, 2825–2838, [https://doi.org/10.1175/1520-0493\(1995\)123<2825:TSCOTT>2.0.CO;2](https://doi.org/10.1175/1520-0493(1995)123<2825:TSCOTT>2.0.CO;2).
- Merlis, T. M., T. Schneider, S. Bordoni, and I. Eisenman, 2013: Hadley circulation response to orbital precession. Part II: Subtropical continent. *J. Climate*, **26**, 754–771, <https://doi.org/10.1175/JCLI-D-12-00149.1>.
- Minobe, S., A. Kuwano-Yoshida, N. Komori, S.-P. Xie, and R. J. Small, 2008: Influence of the Gulf Stream on the troposphere. *Nature*, **452**, 206–209, <https://doi.org/10.1038/nature06690>.
- Mlawer, E. J., S. J. Taubman, P. D. Brown, M. J. Iacono, and S. A. Clough, 1997: Radiative transfer for inhomogeneous atmospheres: RRTM, a validated correlated-k model for the longwave. *J. Geophys. Res.*, **102**, 16 663–16 682, <https://doi.org/10.1029/97JD00237>.
- Ogawa, F., N.-E. Omrani, K. Nishii, H. Nakamura, and N. Keenlyside, 2015: Ozone-induced climate change propped up by the Southern Hemisphere oceanic front. *Geophys. Res. Lett.*, **42**, 10 056–10 063, <https://doi.org/10.1002/2015GL066538>.
- Peña-Ortiz, C., E. Manzini, and M. A. Giorgetta, 2019: Tropical deep convection impact on southern winter stationary waves and its modulation by the quasi-biennial oscillation. *J. Climate*, **32**, 7453–7467, <https://doi.org/10.1175/JCLI-D-18-0763.1>.
- Quintanar, A. I., and C. R. Mechoso, 1995a: Quasi-stationary waves in the Southern Hemisphere. Part I: Observational data. *J. Climate*, **8**, 2659–2672, [https://doi.org/10.1175/1520-0442\(1995\)008<2659:QSWITS>2.0.CO;2](https://doi.org/10.1175/1520-0442(1995)008<2659:QSWITS>2.0.CO;2).
- , and —, 1995b: Quasi-stationary waves in the Southern Hemisphere. Part II: Generation mechanisms. *J. Climate*, **8**,

- 2673–2690, [https://doi.org/10.1175/1520-0442\(1995\)008<2673:QSWITS>2.0.CO;2](https://doi.org/10.1175/1520-0442(1995)008<2673:QSWITS>2.0.CO;2).
- Sampe, T., H. Nakamura, A. Goto, and W. Ohfuchi, 2010: Significance of a midlatitude SST frontal zone in the formation of a storm track and an eddy-driven westerly jet. *J. Climate*, **23**, 1793–1814, <https://doi.org/10.1175/2009JCLI13163.1>.
- Sardeshmukh, P. D., and B. J. Hoskins, 1988: The generation of global rotational flow by steady idealized tropical divergence. *J. Atmos. Sci.*, **45**, 1228–1251, [https://doi.org/10.1175/1520-0469\(1988\)045<1228:TGOGRF>2.0.CO;2](https://doi.org/10.1175/1520-0469(1988)045<1228:TGOGRF>2.0.CO;2).
- Scheff, J., and D. Frierson, 2012: Twenty-first-century multimodel subtropical precipitation declines are mostly midlatitude shifts. *J. Climate*, **25**, 4330–4347, <https://doi.org/10.1175/JCLI-D-11-00393.1>.
- Scott, R. K., and P. H. Haynes, 2002: The seasonal cycle of planetary waves in the winter stratosphere. *J. Atmos. Sci.*, **59**, 803–822, [https://doi.org/10.1175/1520-0469\(2002\)059<0803:TSCOPW>2.0.CO;2](https://doi.org/10.1175/1520-0469(2002)059<0803:TSCOPW>2.0.CO;2).
- Seviour, W. J., D. W. Waugh, L. M. Polvani, G. J. Correa, and C. I. Garfinkel, 2017: Robustness of the simulated tropospheric response to ozone depletion. *J. Climate*, **30**, 2577–2585, <https://doi.org/10.1175/JCLI-D-16-0817.1>.
- Shaw, T., and Coauthors, 2016: Storm track processes and the opposing influences of climate change. *Nat. Geosci.*, **9**, 656–664, <https://doi.org/10.1038/ngeo2783>.
- Sigmond, M., and J. C. Fyfe, 2014: The Antarctic sea ice response to the ozone hole in climate models. *J. Climate*, **27**, 1336–1342, <https://doi.org/10.1175/JCLI-D-13-00590.1>.
- Simpson, I. R., and L. M. Polvani, 2016: Revisiting the relationship between jet position, forced response, and annular mode variability in the southern midlatitudes. *Geophys. Res. Lett.*, **43**, 2896–2903, <https://doi.org/10.1002/2016GL067989>.
- , T. A. Shaw, and R. Seager, 2014: A diagnosis of the seasonally and longitudinally varying midlatitude circulation response to global warming. *J. Atmos. Sci.*, **71**, 2489–2515, <https://doi.org/10.1175/JAS-D-13-0325.1>.
- Small, R. J., R. A. Tomas, and F. O. Bryan, 2014: Storm track response to ocean fronts in a global high-resolution climate model. *Climate Dyn.*, **43**, 805–828, <https://doi.org/10.1007/s00382-013-1980-9>.
- Son, S.-W., and Coauthors, 2018: Tropospheric jet response to Antarctic ozone depletion: An update with Chemistry-Climate Model Initiative (CCMI) models. *Environ. Res. Lett.*, **13**, 054024, <https://doi.org/10.1088/1748-9326/AABF21>.
- Swart, N., and J. Fyfe, 2012a: Observed and simulated changes in the Southern Hemisphere surface westerly wind-stress. *Geophys. Res. Lett.*, **39**, L16711, <https://doi.org/10.1029/2012GL052810>.
- , and —, 2012b: Ocean carbon uptake and storage influenced by wind bias in global climate models. *Nat. Climate Change*, **2**, 47–52, <https://doi.org/10.1038/nclimate1289>.
- Takahashi, K., and D. S. Battisti, 2007: Processes controlling the mean tropical Pacific precipitation pattern. Part II: The SPCZ and the southeast Pacific dry zone. *J. Climate*, **20**, 5696–5706, <https://doi.org/10.1175/2007JCLI1656.1>.
- Taylor, K. E., R. J. Stouffer, and G. A. Meehl, 2012: An overview of CMIP5 and the experiment design. *Bull. Amer. Meteor. Soc.*, **93**, 485–498, <https://doi.org/10.1175/BAMS-D-11-00094.1>.
- Tian, B., and X. Dong, 2020: The double-ITCZ bias in CMIP3, CMIP5, and CMIP6 models based on annual mean precipitation. *Geophys. Res. Lett.*, **47**, e2020GL087232, <https://doi.org/10.1029/2020GL087232>.
- Trenberth, K. E., and J. T. Fasullo, 2018: Applications of an updated atmospheric energetics formulation. *J. Climate*, **31**, 6263–6279, <https://doi.org/10.1175/JCLI-D-17-0838.1>.
- , Y. Zhang, J. T. Fasullo, and L. Cheng, 2019: Observation-based estimate of global and basin ocean meridional heat transport time series. *J. Climate*, **32**, 4567–4583, <https://doi.org/10.1175/JCLI-D-18-0872.1>.
- Wang, L., P. J. Kushner, and D. W. Waugh, 2013: Southern Hemisphere stationary wave response to changes of ozone and greenhouse gases. *J. Climate*, **26**, 10 205–10 217, <https://doi.org/10.1175/JCLI-D-13-00160.1>.
- Watanabe, S., and Coauthors, 2011: MIROC-ESM 2010: Model description and basic results of CMIP5-20c3m experiments. *Geosci. Model Dev.*, **4**, 845–872, <https://doi.org/10.5194/gmd-4-845-2011>.
- Weijer, W., and Coauthors, 2012: The Southern Ocean and its climate in CCSM4. *J. Climate*, **25**, 2652–2675, <https://doi.org/10.1175/JCLI-D-11-00302.1>.
- Wilcox, L., A. Charlton-Perez, and L. Gray, 2012: Trends in austral jet position in ensembles of high- and low-top CMIP5 models. *J. Geophys. Res.*, **117**, D13115, <https://doi.org/10.1029/2012JD017597>.
- Wills, R. C., and T. Schneider, 2018: Mechanisms setting the strength of orographic Rossby waves across a wide range of climates in a moist idealized GCM. *J. Climate*, **31**, 7679–7700, <https://doi.org/10.1175/JCLI-D-17-0700.1>.
- Wirth, V., 1991: What causes the seasonal cycle of stationary waves in the southern stratosphere? *J. Atmos. Sci.*, **48**, 1194–1200, [https://doi.org/10.1175/1520-0469\(1991\)048<1194:WCTSCO>2.0.CO;2](https://doi.org/10.1175/1520-0469(1991)048<1194:WCTSCO>2.0.CO;2).
- Xiang, B., M. Zhao, I. M. Held, and J.-C. Golaz, 2017: Predicting the severity of spurious “double ITCZ” problem in CMIP5 coupled models from AMIP simulations. *Geophys. Res. Lett.*, **44**, 1520–1527, <https://doi.org/10.1002/2016GL071992>.
- Xu, H., M. Xu, S.-P. Xie, and Y. Wang, 2011: Deep atmospheric response to the spring Kuroshio over the East China Sea. *J. Climate*, **24**, 4959–4972, <https://doi.org/10.1175/JCLI-D-10-05034.1>.
- Yao, Y., Z. Zhong, and X.-Q. Yang, 2016: Numerical experiments of the storm track sensitivity to oceanic frontal strength within the Kuroshio/Oyashio extensions. *J. Geophys. Res. Atmos.*, **121**, 2888–2900, <https://doi.org/10.1002/2015JD024381>.
- Zhang, C., 2001: Double ITCZs. *J. Geophys. Res.*, **106**, 11 785–11 792, <https://doi.org/10.1029/2001JD900046>.
- Zhang, G. J., and H. Wang, 2006: Toward mitigating the double ITCZ problem in NCAR CCSM3. *Geophys. Res. Lett.*, **33**, L06709, <https://doi.org/10.1029/2005GL025229>.